TECHNISCHE
UNIVERSITÄT
DRESDEN

Polarized simulations of $W^{\pm}$ or Z boson production with hadronic decays

Bachelor-Arbeit
zur Erlangung des Hochschulgrades
Bachelor of Science
im Bachelor-Studiengang Physik

vorgelegt von

Max Lehmann,
geboren am 10.08.2002 in Hoyerswerda

Institut für Kern- und Teilchenphysik
Fakultät Physik
Bereich Mathematik und Naturwissenschaften
Technische Universität Dresden
2024

CERN-THESIS-2024-296
21/01/2025

Eingereicht am 20. Dezember 2024

1. Gutachter: Dr. Frank Siegert
2. Gutachter: Prof. Dr. Dominik Stöckinger

Abstract

Understanding the polarization of massive vector bosons provides a powerful method to probe the electroweak symmetry breaking mechanism and to test the Standard Model and its potential extensions. This thesis investigates hadronically decaying, polarized $W^{\pm}$ and Z bosons at the LHC energy scale. By analyzing simulated events, the effects of different polarization states on jet substructure observables are explored. The results show that jets stemming from transversely polarized bosons often exhibit distinct two-pronged substructures, while longitudinally polarized bosons yield more isotropic jets. These polarization-dependent patterns manifest in variables such as N-subjettiness, transverse momentum correlation functions, and Fox-Wolfram moments. When attempting to distinguish vector boson jets from QCD jets in the context of highly boosted boson production, a simple mass-window selection on jet candidates offers only limited improvement in identifying vector boson jets. Moreover, relying solely on Fox-Wolfram moments is insufficient. Instead, more advanced jet substructure variables are required to achieve robust discrimination. Overall, this study highlights the sensitivity of jet substructure observables to vector boson polarization and provides insights for the development of future jet tagging algorithms.

Zusammenfassung

Die Untersuchung der Polarisation massereicher Vektorbosonen bietet eine leistungsstarke Methode, um den Mechanismus der elektroschwachen Symmetriebrechung zu erforschen und das Standardmodell sowie mögliche Erweiterungen zu testen. Diese Arbeit untersucht hadronisch zerfallende, polarisierte $W^{\pm}$- und Z-Bosonen bei LHC Energieskalen. Durch die Analyse simulierter Events werden die Auswirkungen unterschiedlicher Polarisationszustände auf Jet-Substruktur-Observablen erforscht. Diese zeigen, dass Jets von transversal polarisierten Bosonen häufig deutlich zweisträngige Substrukturen aufweisen, während longitudinal polarisierte Bosonen eher isotrope Jets erzeugen. Diese polarisationsabhängigen Muster manifestieren sich in Variablen wie der N-Subjettiness, in Impuls-Korrelations-Funktionen und in Fox-Wolfram-Momenten. Bei dem Versuch, Vektorboson Jets in einem Szenario hochenergetisch geboosterter Bosonen von QCD-Jets zu unterscheiden, bietet eine einfache Massen-Fenster-Auswahl für Jet-Kandidaten nur eine begrenzte Verbesserung bei der Identifikation von Vektorboson Jets. Zudem erweist es sich als unzureichend, sich allein auf Fox-Wolfram-Momente zu verlassen. Stattdessen sind fortgeschrittenere Jet-Substruktur-Variablen erforderlich, um eine robuste Unterscheidung zu erreichen. Insgesamt hebt diese Studie die Sensitivität von Jet-Substruktur-Observablen gegenüber der Vektorboson Polarisation hervor und liefert wertvolle Einblicke für die Entwicklung zukünftiger Jet Tagging-Algorithmen.

Contents

1 Introduction

In 2008, humanity activated its most colossal machine to date: the Large Hadron Collider (LHC) [1]. This extraordinary project aims to expand the horizons of scientific understanding by testing the Standard Model of Particle Physics (SM) and exploring physics beyond it. Among the various avenues of investigation, the production of vector bosons stands out as a crucial area of study.

Analyzing the polarization of vector bosons offers a robust method for examining the mechanism of electroweak symmetry breaking. This approach allows for comprehensive tests of both the Standard Model and potential new physics scenarios. Since massive vector bosons appear only as intermediate particles, generating simulated polarized events is essential for understanding how polarization influences experimentally measurable observables.

Special emphasis is placed on the polarization states of $W^{\pm}$ and Z bosons, particularly their longitudinal polarization, which is closely related to the Higgs mechanism and electroweak symmetry breaking. Although leptonic decay channels of $W^{\pm}$ and Z bosons are commonly used for such studies due to the relative ease and precision in detecting charged leptons, hadronic decays are more prevalent. This makes hadronic final states a compelling alternative for polarization studies. Simulating hadronically decaying polarized $W^{\pm}$ and Z bosons is crucial for identifying key observables for future analyses at the ATLAS detector.

Jet substructure variables are particularly suited for these observables, as they are sensitive to the internal structure of the jets. On one hand, they can be used to distinguish between a vector boson jet and a QCD jet, and on the other hand, they are important for identifying the polarization of a vector boson. This is possible because the decay products behave differently under different polarization states of the vector boson.

Studying these observables can aid in the development of a vector boson jet tagger that can also distinguish between the polarization states of the vector boson. Reliable tagging of these jets is important for polarized studies of vector boson scattering processes.

To conduct these studies, this thesis is structured as follows. In chapter 2, the theoretical foundation is established by introducing the Standard Model of particle physics, particularly the Higgs mechanism for the weak gauge bosons and their polarization. Furthermore, the hadronic decays of these vector bosons are examined.

Chapter 3 provides an overview of the experimental setup at the LHC at CERN and the ATLAS detector. Additionally, it introduces the methods used for simulating particle collisions using `SHERPA` and the evaluation of the generated events through the `Rivet` analysis framework.

In chapter 4, the jet configuration for highly boosted hadronically decaying vector bosons is analyzed. The jet from the vector boson and the QCD jet are reconstructed as large-radius jets, known as fat jets. Different methods for identifying the vector boson jet are explored. Additionally, the differential cross section for the observed process is analyzed at various orders of perturbation theory.

Chapter 5 presents the main body of this thesis by investigating the impact of different polarization states of the vector bosons on the resulting jet. Furthermore, the cross section for differently polarized vector bosons is examined.

In chapter 6, a summary of the results and an outlook on future research directions are provided.

2 Theoretical basics

This chapter presents a concise overview of the theoretical foundation needed for this study. It introduces the Standard Model and its associated concepts, including the Higgs mechanism, the polarization of weak gauge bosons, and the hadronic decays of these particles. Section 2.1 and section 2.2 are based on the description in ref. [2].

2.1 The Standard Model of particle physics

The SM currently best describes the fundamental particles and their interactions via forces. Within the SM, particles can be categorized into two main groups: fermions, which constitute matter particles, and bosons, which represent interaction particles.

In the Standard Model, there are twelve fundamental fermions, which are divided into two categories: quarks (purple) and leptons (green), see fig. 2.1. The fermions are further classified into three generations. The first generation includes the up-quark, down-quark, electron, and electron neutrino. These four first-generation particles have two variations that differ only in mass, known as the second and third generations. Each of the twelve fundamental fermions has an antiparticle with the same properties except the inverted charge.

Fermions interact with each other through the four fundamental interactions: gravity, electromagnetism, the strong interaction, and the weak interaction. The weak interaction affects

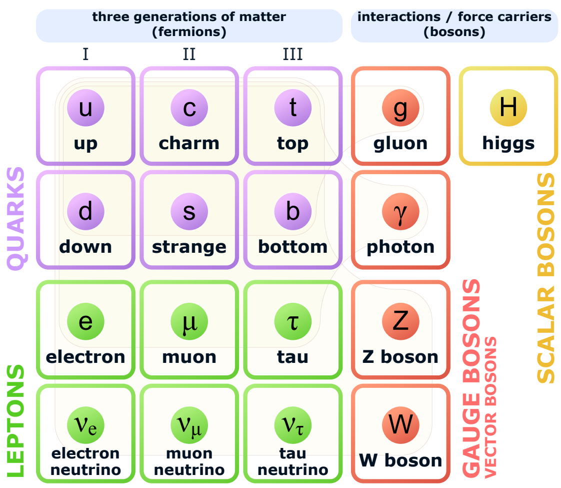

Figure 2.1: The SM of elementary particle physics [3].

all fermions because they all carry the charge of the weak interaction. The electromagnetic interaction, on the other hand, only acts on electrically charged fermions, which means neutrinos are excluded from its influence. All six types of quarks carry a color charge and are therefore influenced by the strong interaction. Due to the nature of this interaction, quarks cannot exist in isolation. Instead, a phenomenon known as confinement ensures that they always combine to form color-neutral particles called hadrons, such as protons and neutrons.

Gravitation is not part of the SM, but the other three fundamental interactions are described by Quantum Field Theories that include corresponding interaction particles known as gauge bosons. The electromagnetic interaction, described by Quantum Electrodynamics (QED), is mediated by a massless photon. The strong interaction, represented by Quantum Chromodynamics (QCD), is conveyed by eight massless gluons, which carry the corresponding charge of the interaction and can therefore interact with one another. The weak interaction is mediated by three massive gauge bosons, namely the W^+, W^-, and Z boson, which can also self-interact because they carry the weak charge.

The massive Higgs boson is the last component of the SM. It was first observed by the ATLAS and CMS experiments at the Large Hadron Collider in 2012. Unlike other bosons in the SM, which have a spin of one, the Higgs boson is a scalar boson, meaning it has a spin of zero. Through the spontaneous symmetry breaking in the Brout–Englert–Higgs mechanism, the weak vector bosons acquire their masses.

2.2 The weak gauge bosons

The weak gauge bosons, which mediate the electroweak interaction, serve as an excellent testing ground for the predictions of the SM. Their unique properties, including the fact that they are massive and thus differ from other gauge bosons, make them crucial candidates for probing the internal consistency and potential extensions of the theory.

2.2.1 The Higgs mechanism

The SM is a Quantum Field Theory that remains invariant under the local gauge symmetry group $\mathrm{SU}(3)_\mathrm{c} \times \mathrm{SU}(2)_\mathrm{L} \times \mathrm{U}(1)_\mathrm{Y}$. Ensuring the internal consistency of the SM requires the implementation of the Higgs Mechanism. Without this mechanism, the electroweak gauge symmetry $\mathrm{SU}(2)_\mathrm{L} \times \mathrm{U}(1)_\mathrm{Y}$ would be explicitly broken by the introduction of masses for the corresponding vector bosons.

To generate masses for the electroweak gauge bosons while preserving gauge invariance, the minimal Higgs model introduces a scalar field ϕ, which transforms as a weak isospin doublet under the symmetry transformations of the $\mathrm{SU}(2)_\mathrm{L}$ group.

The Higgs doublet is expressed as:

$$\phi = \begin{pmatrix} \phi^+ \\ \phi^0 \end{pmatrix} = \frac{1}{\sqrt{2}} \begin{pmatrix} \phi_1 + i\phi_2 \\ \phi_3 + i\phi_4 \end{pmatrix}, \tag{2.1}$$

where the components carry specific quantum numbers. These quantum numbers are given by:

$$\begin{aligned} \phi^+ \quad &\rightarrow \quad \mathrm{I}^3_\mathrm{W} = +\frac{1}{2}, \quad \mathrm{Y} = +\frac{1}{2}, \quad \mathrm{Q} = +1 \\ \phi^0 \quad &\rightarrow \quad \mathrm{I}^3_\mathrm{W} = -\frac{1}{2}, \quad \mathrm{Y} = +\frac{1}{2}, \quad \mathrm{Q} = 0 \end{aligned}$$

Here, I^3_W denotes the third component of the weak isospin, which is associated with the weak interaction. The weak hypercharge Y is defined via the relation $\mathrm{Y} = \mathrm{Q} - \mathrm{I}^3_\mathrm{W}$, where Q represents the electric charge. The scalar doublet ϕ contains complex fields: the charged component ϕ^+ and the neutral component ϕ^0, differing by one unit of electric charge.

The Lagrangian for the Higgs sector is given by:

$$\mathcal{L} = \underbrace{(\partial_\mu \phi)^\dagger (\partial^\mu \phi)}_{\text{kinetic term}} \underbrace{-\mu^2 \phi^\dagger \phi - \lambda(\phi^\dagger \phi)^2}_{\text{Higgs potential}}. \tag{2.2}$$

For the potential to spontaneously break symmetry, the parameter μ^2 must be negative. This condition leads to a non-zero vacuum expectation value v for the Higgs field, gained by expanding the field around the vacuum state:

$$\phi = \frac{1}{\sqrt{2}} \begin{pmatrix} 0 \\ v + h(x) \end{pmatrix}. \tag{2.3}$$

In this expression, $h(x)$ represents the physical Higgs boson field corresponding to fluctuations around the vacuum expectation value. The explicit choice of the vacuum state spontaneously breaks the symmetry of the Lagrangian.

To incorporate the local electroweak gauge symmetry into the theory, the ordinary covariant derivatives in the Lagrangian from eq. (2.2) are replaced by the new covariant derivatives:

$$D_\mu = \partial_\mu - i g_\mathrm{W} \frac{1}{2} \boldsymbol{\sigma} \cdot \mathbf{W}_\mu - i g_\mathrm{Y} \frac{1}{2} B_\mu, \tag{2.4}$$

where g_W and g_Y are the coupling constants for $\mathrm{SU(2)_L}$ and $\mathrm{U(1)_Y}$, respectively. $\boldsymbol{\sigma}$ represents the Pauli matrices, which serve as the generators for $\mathrm{SU(2)_L}$. The gauge fields $\mathbf{W}_\mu = (W^1_\mu, W^2_\mu, W^3_\mu)$ are associated with $\mathrm{SU(2)_L}$, while B_μ is the gauge field associated with $\mathrm{U(1)_Y}$. Substituting the covariant derivative into the kinetic term of the Lagrangian and expanding around the vacuum expectation value as shown above leads to mass terms for the electroweak gauge bosons. The resulting masses are:

$$m_{\mathrm{W}} = \frac{1}{2} g_{\mathrm{W}} v, \quad m_{\mathrm{Z}} = \frac{1}{2} v \sqrt{g_{\mathrm{W}}^2 + g_{\mathrm{Y}}^2}, \quad m_{\mathrm{A}} = 0. \tag{2.5}$$

Here, m_{W} and m_{Z} are the masses of the $W^{\pm}$ and Z bosons, respectively. The mass of the photon, m_{A}, remains zero since the $\mathrm{U}(1)_{\mathrm{Y}}$ gauge symmetry is preserved after symmetry breaking.

After spontaneous symmetry breaking, the Higgs mechanism results in one massive scalar boson, identified as the physical Higgs boson $h(x)$, and three massless Goldstone bosons. The additional degrees of freedom represented by the Goldstone bosons are realized as longitudinal polarization states for the massive gauge bosons.

2.2.2 Polarization

To define the polarization states of a particle, a suitable basis must first be selected. A natural choice is the helicity basis, where the helicity h is defined as the projection of the spin $\mathbf{S}$ of the particle on its direction of flight described by the momentum $\mathbf{p}$ of the particle.

$$h = \frac{\mathbf{S} \cdot \mathbf{p}}{|\mathbf{p}|} \tag{2.6}$$

It is further normalized by dividing by $|\mathbf{p}|$. Since the weak vector bosons are massive spin-1 particles, they have three helicity states: -1, 0, and 1. With the helicity eigenstates, the different polarization states of a particle can be defined.

The Lagrangian for a massive vector boson is given by

$$\mathcal{L} = \underbrace{-\frac{1}{4} F^{\mu\nu} F_{\mu\nu}}_{\text{kinetic term}} + \underbrace{\frac{1}{2} m^2 B^{\mu} B_{\mu}}_{\text{mass term}}, \tag{2.7}$$

where B^{μ} is the four-vector potential and the field-strength tensor is defined as

$$F^{\mu\nu} = \partial^{\mu} B^{\nu} - \partial^{\nu} B^{\mu}. \tag{2.8}$$

The Euler-Lagrange equations derived from this Lagrangian yield the Proca equation. Applying the spacetime derivative to the Proca equation results in

$$\partial_{\mu}(\underbrace{(\Box + m^2) B^{\mu} - \partial^{\mu}(\partial_{\nu} B^{\nu})) = 0}_{\text{Proca equation}} \quad \Leftrightarrow \quad \underbrace{\partial_{\mu} B^{\mu} = 0}_{\text{Lorenz condition}} . \tag{2.9}$$

With the Lorenz condition in eq. (2.9), the Proca equation simplifies to

$$(\Box + m^2)B^\mu = 0. \tag{2.10}$$

Assuming a plane wave solution of the form

$$B^\mu = \epsilon^\mu e^{-iq\cdot x}, \tag{2.11}$$

where ϵ^μ is the polarization four-vector, q^μ is the boson four-momentum, and x^μ is the spacetime position, the polarization states of the massive vector boson can be analyzed.

The Lorenz condition sets a constraint on the polarization vectors, reducing the four degrees of freedom to three physical polarization states. For a massive spin-1 boson moving in the z-direction, these polarization states can be chosen as two transverse circular polarizations and one longitudinal polarization. The circular polarization states are

$$\epsilon^\mu_- = \frac{1}{\sqrt{2}}(0, 1, -i, 0) \quad \text{and} \quad \epsilon^\mu_+ = -\frac{1}{\sqrt{2}}(0, 1, i, 0), \tag{2.12}$$

while the longitudinal polarization state, which is unique to massive vector bosons, is given by

$$\epsilon^\mu_\mathrm{L} = \frac{1}{m}(p_\mathrm{z}, 0, 0, E). \tag{2.13}$$

The relationship between the Higgs mechanism and the polarization states of the weak gauge bosons is fundamentally established through the process of spontaneous symmetry breaking. As the Higgs field acquires a non-zero vacuum expectation value, the electroweak symmetry is broken, resulting in the gauge bosons obtaining mass. This mass generation is intrinsically linked to the emergence of longitudinal polarization states for the massive vector bosons. Specifically, the degrees of freedom that were originally associated with the Goldstone bosons in the Higgs field are absorbed, providing the necessary longitudinal components to the $W^\pm$ and Z bosons. Consequently, the presence of these additional polarization states serves as a direct consequence of the Higgs mechanism.

2.3 Hadronic decay of massive vector bosons

This thesis examines the hadronic decay modes of the weak gauge bosons. While leptonic decay channels of the $W^\pm$ and Z bosons are commonly utilized in analyses, the significantly higher branching ratios of hadronic decays make hadronic final states a compelling alternative. The branching ratios for hadronic decays are 67.41 % for the $W^\pm$ bosons and 69.91 % for the Z boson [4]. However, the challenge with hadronic decays is that they produce collimated sprays of particles known as jets. Accurately reconstructing these jets from the multitude of particles generated in collisions presents a substantial challenge.

2.3.1 Single $W^{\pm}$ and Z boson production in association with a jet

This thesis investigates the production of single $W^{\pm}$ and Z bosons in association with a jet. In the final state, a QCD jet accompanies the decay products of the vector boson. The presence of this jet is crucial for generating highly boosted vector bosons, which can then be analyzed in detail. A highly boosted vector boson is characterized by a large transverse momentum p_T.

The leading order (LO) process for this production has a coupling order of $\mathcal{O}(\alpha_{\mathrm{S}}\alpha_{\mathrm{EW}}^2)$ and result in a quark-antiquark pair alongside a QCD jet in the final state:

$$pp \to W^{\pm} + j \to q\bar{q}' + j, \quad pp \to Z + j \to q\bar{q} + j, \quad \text{and} \quad pp \to \gamma + j \to q\bar{q} + j.$$

The LO Feynman diagrams for this process are depicted in fig. 2.2. At the core of these interactions, two initial-state partons from the colliding protons couple to a $W^{\pm}$ boson, Z boson, or photon, accompanied by the radiation of a gluon or quark. Subsequently, the vector boson decays hadronically into a quark-antiquark pair.

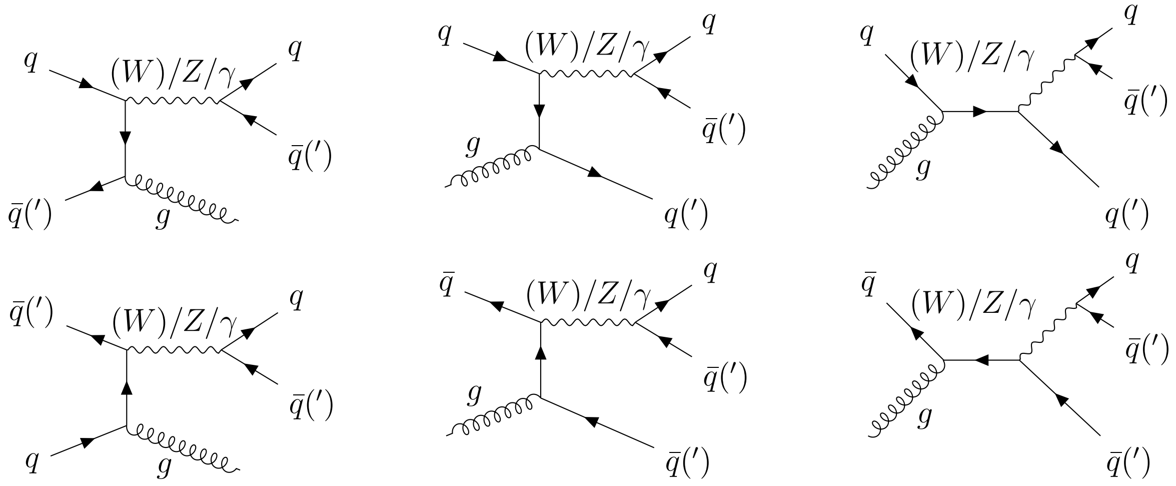

Figure 2.2: LO Feynman diagrams for single $W^{\pm}$ and Z + jet production. Gluons are denoted as g, q is an up- or down-type quark and $\bar{q}, \bar{q}'$ their anti-particle. Note, that only the $W^{\pm}$ boson changes the flavor of the quarks, denoted with (').

The next to leading QCD order (NLO) process has a coupling order of $\mathcal{O}(\alpha_{\mathrm{S}}^2\alpha_{\mathrm{EW}}^2)$. Two example Feynman diagrams contributing to these NLO correction are depicted in fig. 2.3. These corrections can be divided into virtual loop corrections and real corrections that add to the final state. Real correcrions contain an additional final state emission compared to the LO process. Virtual loop corrections contain a closed loop and therefore do not change the final state.

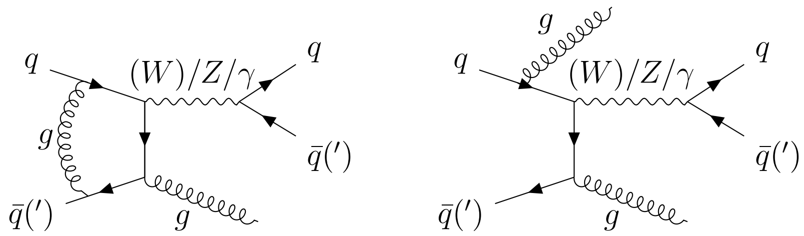

Figure 2.3: Example Feynman diagrams contributing to the NLO corrections for the single $W^{\pm}$ and Z + jet production.

The single vector boson production with an associated jet in the final state has one of the highest cross sections for electroweak boson production, making it a significant background for various Standard Model processes at the LHC. It is particularly noteworthy because the study of jet properties arising from polarized massive vector bosons is crucial for vector boson scattering analyses. Many theories that extend beyond the SM predict the existence of new particles with masses in the TeV range. Some of these particles are expected to decay into final states that include $W^{\pm}$ or Z bosons. Since the masses of the $W^{\pm}$ and Z bosons are roughly an order of magnitude smaller than those of their hypothetical parent particles, these decays result in $W^{\pm}$ and Z bosons that are highly boosted in the laboratory frame. The ability to identify and reconstruct $W^{\pm}$ and Z bosons from such highly energetic jets is crucial for enhancing the sensitivity of searches for new phenomena [5].

2.3.2 Hadronization and jets

In this thesis, a highly boosted, massive gauge boson that undergoes a hadronic decay is considered. Due to color confinement in QCD, the energetic quarks produced in the decay cannot travel as free particles. Instead, they form a collimated bunch of color-neutral hadrons, commonly referred to as a jet. The process by which a high energy quark-antiquark pair transforms into a group of colorless hadrons is known as hadronization.

The precise mechanism of hadronization cannot be fully derived from first principles. However, a qualitative description can be provided in the center-of-mass frame, where the two quarks are produced back-to-back [2]. As the distance between the quarks increases, the color field forms a flux tube with an energy density of approximately 1 GeV/fm. When the energy stored in this flux tube reaches a critical value, the production of a new quark-antiquark pair becomes energetically favorable. This process continues until the energy is sufficiently low for the quarks to combine and form colorless hadrons.

3 Setup

This chapter presents a concise overview of the design and operating principles of CERN's accelerator complex, focusing on the LHC and the ATLAS detector. It specifically introduces the coordinate system used at the ATLAS detector. Furthermore, an outline of Monte Carlo event generation using `SHERPA 3` and event analysis with `Rivet 4` is provided.

3.1 The Large Hadron Collider

The LHC at CERN is the most powerful particle accelerator in the world. Located underground near Geneva, this 27-kilometer-long collider is designed to facilitate proton-proton collisions at center-of-mass energies of up to 14 TeV. This thesis focuses exclusively on experiments conducted at a center-of-mass energy of 13 TeV, consistent with the conditions of Run-2 from early 2015 to late 2018.

Particle accelerators generate electromagnetic fields to boost particles to higher energies. Achieving these enormous energies requires accelerating particles over longer distances, which is why accelerators are constructed with a circular design. This design requires a magnetic field to continuously bend the particle paths, keeping them on course. In the LHC, two particle beams circulate in opposite directions, each carrying an energy of up to 6.5 TeV in Run-2.

To reach these high energies, protons must first pass through a series of pre-accelerators, as illustrated in fig. 3.1. The acceleration process begins in a linear accelerator (LINAC), where negative hydrogen ions are accelerated to 160 MeV. Subsequently, electrons are stripped from these ions, leaving behind protons that enter the Proton Synchrotron Booster (PSB). Upon exiting the PSB, the protons have been accelerated to 2 GeV. Next, they are injected into the Proton Synchrotron (PS), where they reach a beam energy of 26 GeV. In the final stage before entering the LHC, the protons pass through the Super Proton Synchrotron (SPS), where they are accelerated to 450 GeV [7].

Once injected into the LHC, the protons achieve their maximum beam energy after approximately 20 minutes. They then circulate at nearly the speed of light, completing over 11.000 laps around the ring each second [8].

The beams collide within the straight sections of the LHC, where the four major experiments -ATLAS (A Toroidal LHC ApparatuS), CMS (Compact Muon Solenoid), ALICE (A

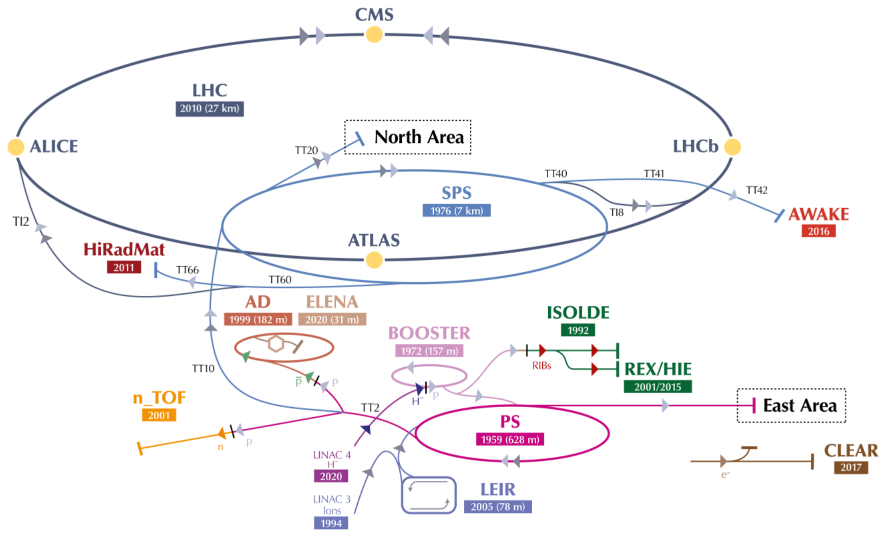

Figure 3.1: The LHC and its pre-accelerators in the CERN complex [6]. The protons that are to be accelerated in the LHC take the following path: LINAC 4 - BOOSTER - PS - SPS - LHC

Large Ion Collider Experiment), and LHCb (Large Hadron Collider beauty experiment)- are located. Both the ATLAS and the CMS experiments are designed for high-precision, general-purpose measurements and serve to cross-validate each other's results, ensuring accuracy and reliability in their findings.

3.2 The ATLAS detector

The particle beams intersect at the center of the ATLAS detector, where they collide and interact. The primary objective is to capture and measure as many decay processes as possible. The ATLAS detector itself is cylindrical, measuring 46 m in length and 25 m in diameter, and has a total mass of 7.000 t [9].

3.2.1 Inner structure

The ATLAS detector comprises six distinct substructures, each tailored for a specific function. These detector systems are arranged in concentric layers surrounding the collision point, as illustrated in fig. 3.2.

The innermost layer consists of three detectors designed to track the trajectories of electrically charged particles. The particles traverse a magnetic field parallel to the beam axis, generated by the central solenoid magnet. As electrically charged particles move through this magnetic field, their paths curve, enabling precise measurements of their momentum and electric charge based on the degree of curvature.

Almost all particles are absorbed by the calorimeter system after passing through the

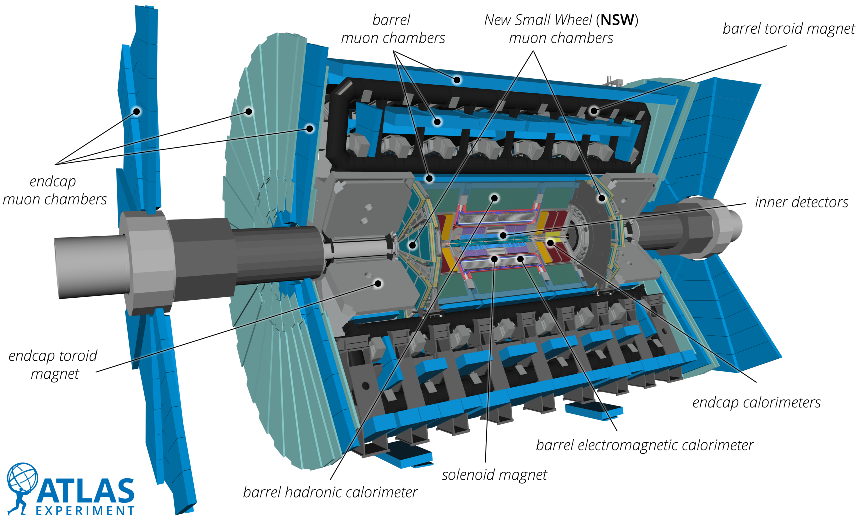

Figure 3.2: Schematic illustration of the ATLAS experiment [10]

inner detector. In the calorimeters, the energy of these particles is deposited and measured. Electromagnetic Calorimeters are designed to measure the energy of electrons and photons by detecting the electromagnetic showers they produce upon interacting with the detector material. Hadronic Calorimeters are responsible for measuring the energy of hadrons that penetrate the electromagnetic calorimeter. As hadrons interact with atomic nuclei, they generate hadronic showers, which are detected and measured.

To accurately identify and measure the momentum of muons, a specialized detector system is employed. Due to their large mass, muons can pass through the calorimeters without being absorbed. This system precisely measures the position of muons and uses the toroid magnet system to bend their trajectories, allowing for accurate determination of their momentum.

3.2.2 Coordinate system

In the ATLAS detector, a right-handed Cartesian coordinate system is set with its origin at the interaction point. The z-axis aligns with the anti clockwise beam direction, while the x- and y-axes are transverse to the beam. Specifically, the x-axis points from the interaction point toward the center of the LHC, and the positive y-axis points upward.

To simplify the description of particle directions, spherical coordinates are employed, as illustrated in fig. 3.3. In this system, the polar angle ϕ is defined relative to the x-axis, and the azimuthal angle θ is measured with respect to the beam direction along the z-axis.

The pseudorapidity η is defined as:

$$\eta = -\ln\left(\tan\frac{\theta}{2}\right). \tag{3.1}$$

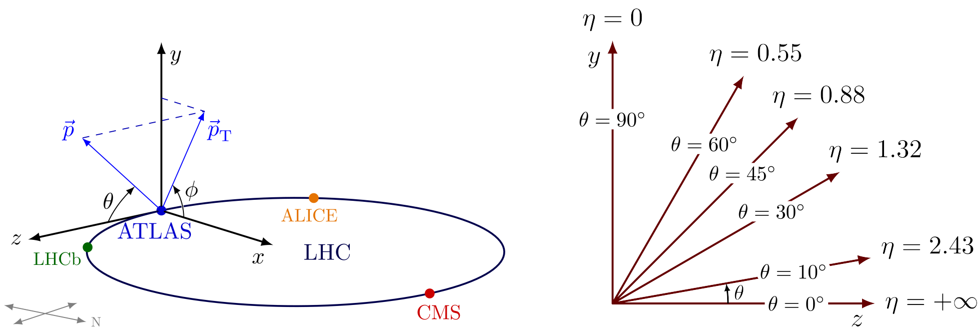

Figure 3.3: Left: The coordinate system of the ATLAS experiment within the context of the LHC [11]. $\mathbf{p}$ represents the total momentum of a particle after the collision, and $\mathbf{p}_\mathrm{T}$ its transverse component. Note that $\mathbf{p}_\mathrm{T}$ is invariant under Lorentz boosts along the z-axis. Right: Various values of the pseudorapidity η [12].

A pseudorapidity of zero means that the particle is perpendicular to the beam axis and a pseudorapidity approaching infinity means, that it is parallel to the beam axis, see fig. 3.3. The pseudorapidity is particularly useful because differences, denoted as $\Delta\eta$, remain invariant under boosts along the beam direction for massless particles. This invariance is commonly utilized to define the distance in pseudorapidity-azimuthal angle space, ΔR, given by:

$$\Delta R = \sqrt{(\Delta\eta)^2 + (\Delta\phi)^2} \tag{3.2}$$

The ATLAS coordinate system allows for precise three-dimensional tracking of particle trajectories and interactions by integrating Cartesian and spherical coordinates and employing pseudorapidity for angular measurements. The distance ΔR in η-ϕ space is essential for analyzing the spatial separation between particles and jets in collider events.

3.3 Event generation and analysis framework

Proton-proton collisions can be simulated using Monte Carlo event generators, which serve as essential tools bridging the gap between experimental observations and theoretical models in particle physics. In this thesis, high-energy interactions are simulated using `SHERPA` (Simulation of High-Energy Reactions of PArticles) [13]. The generated events are subsequently analyzed with the `Rivet` framework (Robust Independent Validation of Experiment and Theory) [14].

3.3.1 Monte-Carlo event generation with SHERPA

In fig. 3.4, a sketch of an event at the LHC, highlighting its different stages, is shown. The process starts with the hard scattering, represented by the central red dot, which is calculated using fixed-order perturbation theory [15]. Important features of the process of interest, such as the production and decay of gauge bosons or the number of hard QCD jets, can be included here.

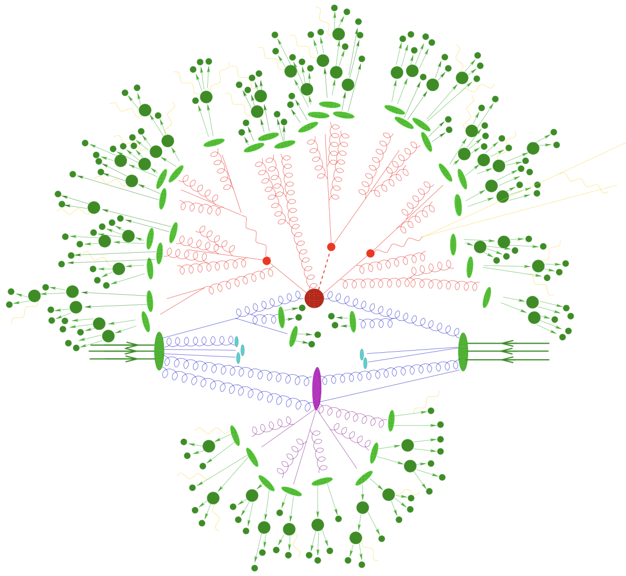

Figure 3.4: Visualisation of a particle collision in `SHERPA` [13].

At the high energy of the hard scattering, the partons inside the colliding protons act almost like free particles. This allows them to emit gluons even before the hard scattering occurs [16]. These gluons can produce more gluons, creating a chain reaction known as the initial-state parton shower (blue). In this thesis, all final-state particles of the hard scattering are QCD partons. As a result, they trigger a parton shower following the hard scattering (red).

When the asymptotically free colored partons lose enough of their energy, they become confined in colorless hadrons, that are decayed further into more stable particles (green). In events with electromagnetically charged particles QED radiation (yellow) is simulated in Monte-Carlo generators. More than one parton pair of the incoming protons can interact, the additional interactions are referred to as the underlying event (purple).

General setup

To implement the key characteristics of the process of interest, Run-Cards are defined as input to `SHERPA` (see B). All simulated events in this thesis are based on proton-proton collisions, where each beam has an energy of 6.5 TeV, as mentioned in section 3.1. Quarks in protons interact through gluon exchange, resulting in quark momentum distributions modeled by Parton Distribution Functions (PDFs), which can be set individually.

To simulate events involving unstable particles such as the $W^{\pm}$ or Z bosons (see their widths in table 3.1), the narrow-width approximation is employed. In this approach, the vector boson production subprocess (referred to as the hard process) and the subsequent vector boson decays (referred to as hard decays) are treated separately [16].

For the studies in this thesis, the massive vector bosons have to be highly boosted, hence only events where they have a transverse momentum p_T greater than 200 GeV, are generated.

boson	**mass** [GeV]	**width** [GeV]
$W^{\pm}$	80.3692 ± 0.0133	2.085 ± 0.042
Z	91.1880 ± 0.0020	2.4955 ± 0.0023

Table 3.1: Masses and decay widths of the weak gauge bosons [4].

3.3.2 The Rivet analysis framework and relevant observables

The events generated by `SHERPA` are analyzed using `Rivet`, an object-oriented `C++` framework for analysis algorithms. To address the specific requirements of this thesis, custom `Rivet` routines have been developed to analyze and visualize the processes of interest.

General configuration

To obtain realistic results, the phase space is restricted to the phase space covered by the ATLAS detector. Consequently, a cut on the pseudorapidity, $|\eta| < 4.5$, is necessary. Additionally, only a fully hadronic final state is of interest, necessitating the exclusion of events in which charged leptons appear in the final states.

Jet selection

To identify a jet in an event, the anti-k_t jet algorithm is employed, which clusters individual particles together [17]. The algorithm is applied with a radius of $R = 1.0$ to identify „fat jets“ or „large radius jets,“ while a radius of $R = 0.4$ is used to find „small jets.“ The kinematic characteristics of a jet, such as its transverse momentum, mass, pseudorapidity, or azimuthal distribution, are calculated based on the properties of the particles that belong to that jet. For fat jets, a transverse momentum (p_T^J) greater than 400 GeV and a mass (m^J) greater than 40 GeV are required. Similarly, for small jets, a p_T^j greater than 25 GeV is necessary. If no fat jet or small jet meets these requirements the event will be vetoed.

Jet substructure variables

Fat jets are analyzed using various substructure variables. These variables are not only useful for discriminating vector boson jets from the QCD jets but can also exhibit sensitivity to different polarization states of the vector boson.

- The **Fox-Wolfram moments** [18], denoted as H_l, are defined by:

$$H_l = \sum_{i,j} \frac{|\mathbf{p}_i||\mathbf{p}_j|}{E^2} P_l(\cos\theta_{ij}) \tag{3.3}$$

In this equation, the summation extends over all pairs of jet constituents i, j. The momenta of particles i and j are represented by $\mathbf{p}_i$ and $\mathbf{p}_j$, respectively. The opening angle between these particles is denoted by θ_{ij}. The total energy of all particles in the center-of-mass frame of the jet is E. P_l represents the Legendre polynomials.

- The **N-subjettiness** [19] variable, τ_N, is expressed as:

$$\tau_N = \frac{1}{d_0} \sum_k p_{T,k} \min\{\Delta R_{1,k}, \Delta R_{2,k}, \ldots, \Delta R_{N,k}\} \tag{3.4}$$

In this expression, $\Delta R_{j,k} = \sqrt{(y_j - y_k)^2 + (\phi_j - \phi_k)^2}$ denotes the distance in the rapidity-azimuthal plane between sub-jet j and particle k. The rapidity is defined as:

$$y = \frac{1}{2} \ln\left(\frac{E + p_z}{E - p_z}\right) \tag{3.5}$$

where E is the energy and p_z the z-component of a sub-jet or a particle The normalization factor d_0 is defined as $d_0 = \sum_k p_{T,k} R_0$, where R_0 is the radius parameter for the anti-k_t jet clustering algorithm.

- The **transverse momentum correlation functions** [20] are defined by:

$$\mathrm{ECF}(N) = \sum_{i_1 < i_2 < \cdots < i_N \in J} \prod_{a=1}^{N} p_{T,i_a} \prod_{b=1}^{N-1} \prod_{c=b+1}^{N} R_{i_b i_c}. \tag{3.6}$$

In this expression, the sum is taken over all combinations of N distinct particles $i_1 < i_2 < \cdots < i_N$ within the jet J. The transverse momentum of particle i_a is denoted by p_{T,i_a}. The term $R_{ij} = (y_i - y_j)^2 + (\phi_i - \phi_j)^2$ represents the squared distance between particles i and j in the rapidity-azimuthal angle plane.

The N-subjettiness and the transverse momentum correlation functions are implemented as described in ref. [21].

4 Unpolarized studies

In this chapter, unpolarized events with hadronically decaying, highly boosted, massive vector bosons are analyzed. First, a short analysis of the kinematic structure of the events is provided. Then, the cross sections of processes at different perturbation orders are compared. In addition, two different approaches for identifying the vector boson jet are evaluated.

4.1 Jet configuration

This section presents an analysis of events from the central ATLAS sample [22] for the production of $W^\pm$ bosons in association with a jet. Similar observations could be made for the hadronic decays of boosted Z bosons. The analysis level cuts are chosen as described in section 3.3.2.

The final state of the LO process is composed of a quark-antiquark pair from the vector boson decay, along with an additional quark or gluon, see section 2.3.1. This configuration results in the formation of hadronic jets, which are reconstructed using the anti-k_t jet clustering algorithm. Notably, the quark-antiquark pair originating from the highly boosted $W^\pm$ boson is produced collinearly in the lab frame, leading to its reconstruction as one fat jet. Due to momentum conservation, in the center-of-mass frame, the $W^\pm$ boson's decay products and the additional parton at leading order are produced back-to-back, each carrying approximately the same transverse momentum.

In most events, both the decay products and the additional recoil parton are reconstructed as fat jets, see fig. A.1. In events with two fat jets, J1 is identified as the leading fat jet based on transverse momentum, while J2 is identified as the sub-leading fat jet. The differential cross section of $\Delta R^{\mathrm{J1,J2}}$, shown in the upper left panel of fig. 4.1, confirms that the two fat jets are produced back-to-back. In terms of the pseudorapidity-azimuthal distance ΔR as defined in eq. (3.2), the difference in pseudorapidity $\Delta\eta$ is approximately zero, leading to the approximation $\Delta R \approx \Delta\phi$. This leads to a peak at $\Delta R^{\mathrm{J1,J2}} \approx \Delta\phi^{\mathrm{J1,J2}} \approx \pi$. In most cases, there are three small jets (see fig. A.1) labeled j1, j2, and j3. They are also sorted by p_{T}. The differential cross section for $\Delta R^{\mathrm{J1,j1}}$ in the upper right panel of fig. 4.1 shows that the leading small jet j1 is aligned with one of the fat jets, either parallel or antiparallel to J1. In the lower left panel of fig. 4.1, the differential cross section for $\Delta R^{\mathrm{j1,j2}}$ shows a clear peak at $\Delta R^{\mathrm{j1,j2}} \approx \pi$. This indicates that j2 points preferably in the opposite direction of j1.

A similar shape is seen for $\Delta R^{\mathrm{j1,j3}}$ in the bottom right histogram of fig. 4.1, although the maximum is broader and a small peak at approximately $\Delta R^{\mathrm{j1,j3}} \approx 0.4$ is present. This small peak arises due to the possibility of more complex configurations when additional small jets are reconstructed. However, since j1 and j2 have higher priority and cannot overlap with j3, the jets can only approach each other as closely as defined by the anti-k_t radius parameter for small jets.

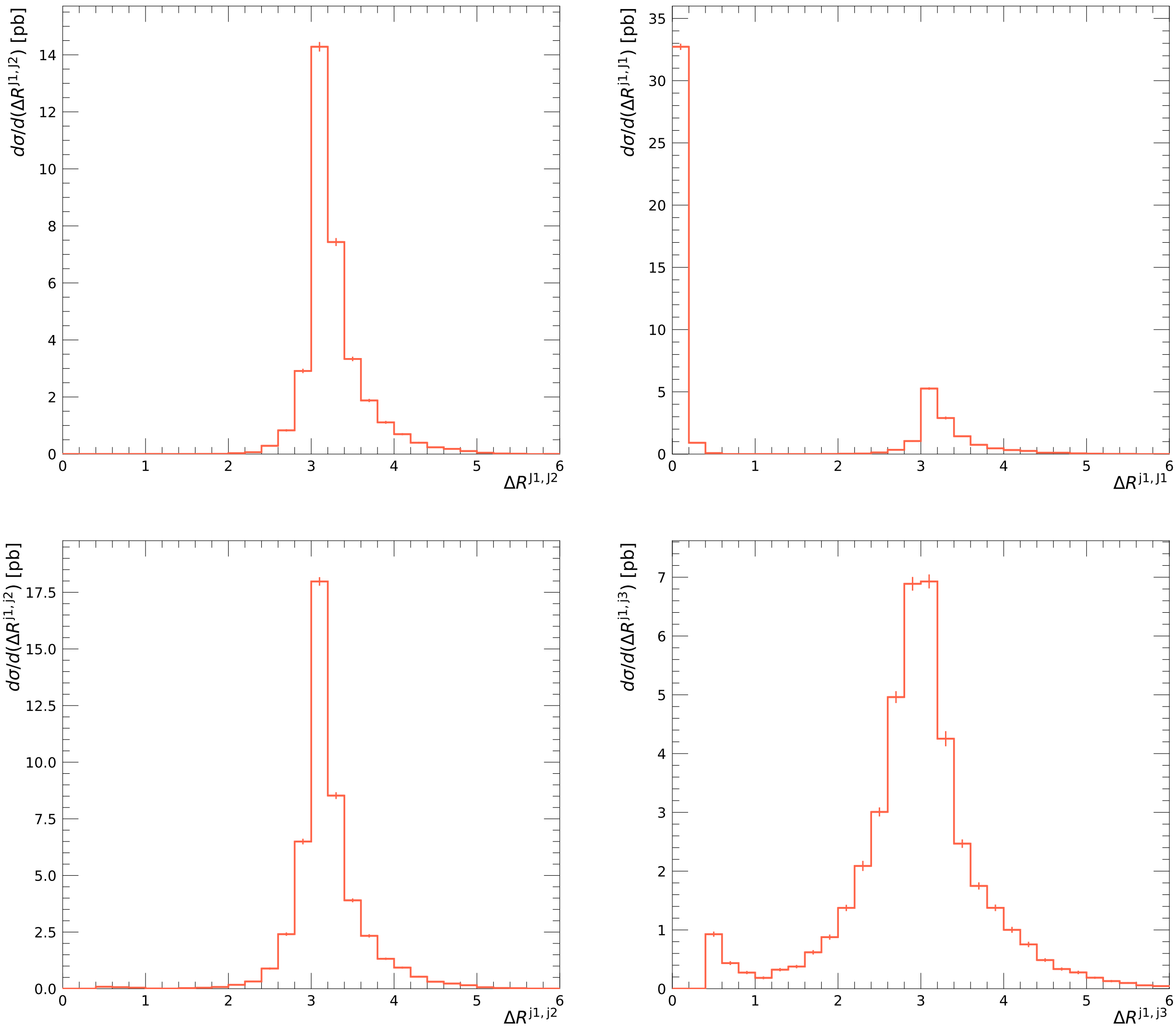

Figure 4.1: ΔR between different jet configurations: upper left: leading fat jet and sub-leading fat jet; upper right: leading fat jet and leading small jet; lower left: leading small jet and sub-leading small jet; lower right: leading small jet and sub-sub-leading small jet.

In summary, the hadronic event structure is inherently complex because the ATLAS detector only directly measures hadronic jets, rather than the individual final-state particles from the hard process. The resulting high jet multiplicities further complicate the analysis. A key challenge, therefore, is to identify which fat jet originates from the $W^{\pm}$ boson decay.

4.2 Impact of higher order corrections

In this section, the influence of adding more jets in the final state of the hard process is analyzed for the single $W^{\pm}$ production with an associated jet. The LO process for boosted $W^{\pm}$ boson production contains one additional jet from the recoil parton in the final state, and is denoted as "1j@LO." There are two different methods for incorporating higher order effects into the LO sample, called matching and merging. Matching is NLO exact, whereas merging is an approximation. The central ATLAS sample is produced with up to two jets at NLO and up to five jets at LO. Therefore it accounts for the highest order correction used in this thesis and a reference for the quality for the lower order simulations.

The events for the LO ("1j@LO") sample and the "1j@NLO+2-3j@LO" sample are generated with `SHERPA 3`, whereas events for the "1-2j@NLO+3-5j@LO" central ATLAS sample are generated with `SHERPA 2`. The integrated cross sections for these processes at analysis level can be found in table 4.1.

process	**cross section [**pb**]**
1-2j@NLO+3-5j@LO	6.97 ± 0.05
1j@NLO+2-3j@LO	7.78 ± 0.02
1j@LO	4.08 ± 0.02

Table 4.1: Integrated cross sections along with the statistical error for different samples at analysis level.

The integrated cross section at the analysis level for the LO process is approximately 50% smaller compared to the "1j@NLO+2-3j@LO" sample. The cross section for the "1-2j@NLO+3-5j@LO" sample is about 10% larger than for the "1j@NLO+2-3j@LO" sample. It can be seen, that the incorporation of higher perturbation orders for the LO process leads to an increase of the cross section. But the "1j@NLO+2-3j@LO" sample shows a higher cross section than the central ATLAS sample. This discrepancy may arise because not all conditions of the central ATLAS sample were fully replicated, such as different correction accuracies. Furthermore, differences in default configurations between `SHERPA2` and `SHERPA 3` could also contribute to this effect.

The differential cross sections for the various samples are shown in fig. 4.2. To highlight differences in their distributions, each cross section is normalized to unity. The ratio plot illustrates how the LO sample and the “1j@NLO+2-3j@LO” sample deviate from the central ATLAS sample. The upper left plot of fig. 4.2 shows the mass of the $W^{\pm}$ boson jet, that is assigned using the truth information about the $W^{\pm}$ boson from the simulation. It can be seen that the shapes of the events from the central ATLAS sample show a clear difference to the events generated at lower perturbation orders. Also a seperation at higher masses of the LO and the "1j@NLO+2-3j@LO" sample is visible. The other plots of fig. 4.2 show the mass

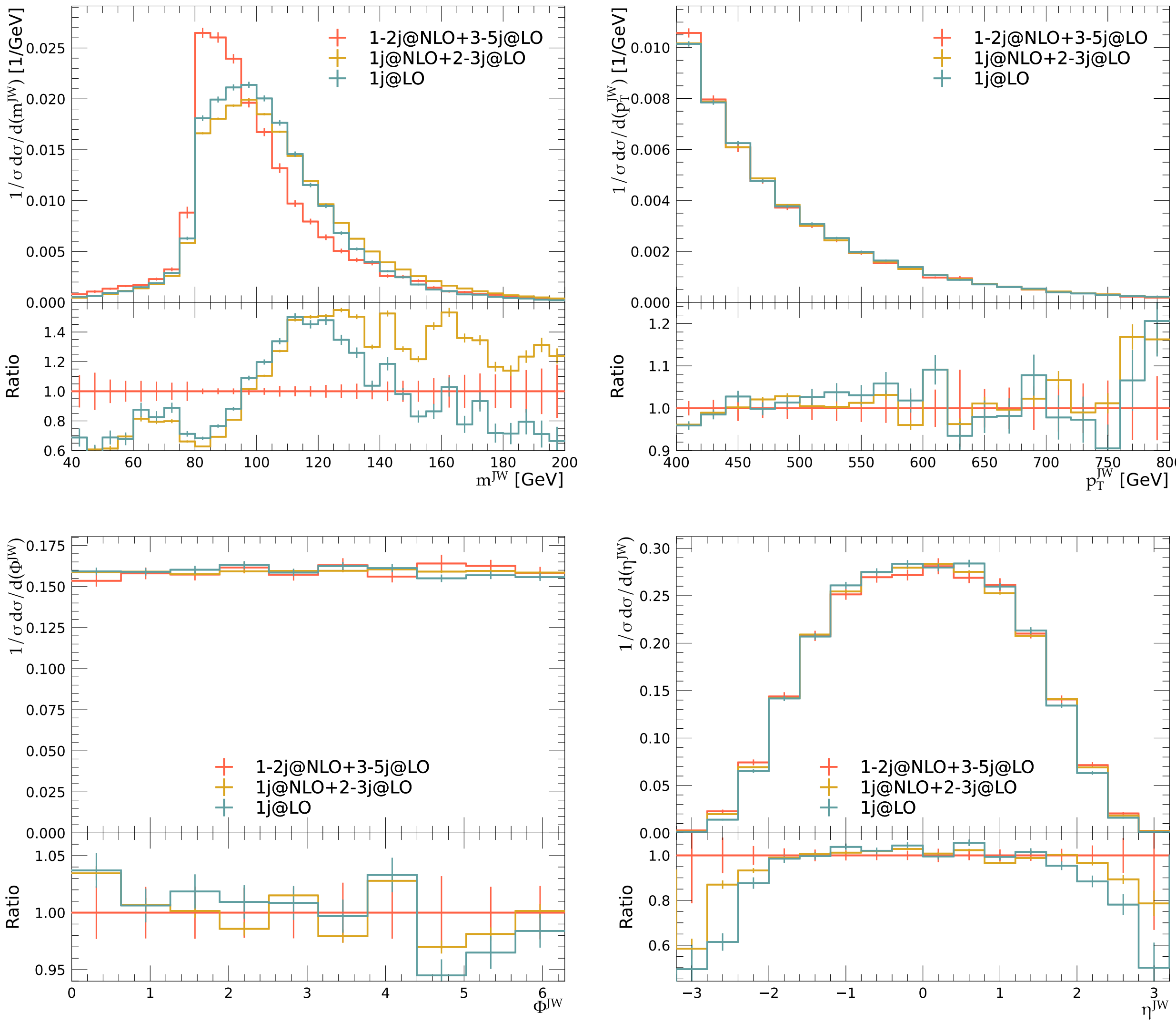

Figure 4.2: Normalized differential cross section for kinematic variables of the $W^{\pm}$ boson jet for different samples along with their ratio. Top left: mass m^{JW}, top right: transverse momentum p_T^{JW}, bottom left: azimuthal angle ϕ^{JW}, bottom right: pseudorapidity η^{JW}.

m^{JW}, azimuthal angle ϕ^{JW} and the pseudorapidity η^{JW} each of the $W^{\pm}$ boson jet. They show a good agreement of the lower order samples with the central ATLAS sample.

It is noticeable, that the errors for the central ATLAS sample are higher than for the other samples. For each of these samples a similar number of events is produced, therefore a comparable statistical error is expected. Cause of the bigger uncertainties could be, that for the central sample an enhance function is applied at generation level that enhances unfavorable sections of the phase space for this study. Enhance functions modify the event generation probability by multiplying a factor, which increases the likelihood of producing events within specific regions of the phase space. Note that by comparing events from different versions of `SHERPA`, this study can serve as a validation of `SHERPA 3`.

4.3 Identification of the $W^{\pm}$ boson fat jet

A direct identification of fat jets originating from the $W^{\pm}$ boson is not straightforward. First the mass of the $W^{\pm}$ boson jet and then a jet substructure variable will be explored in this section with the aim of achieving this distinction. Leveraging the particle identification information provided by SHERPA for every particle in the event, the jet associated with the $W^{\pm}$ boson is identified by verifying that the pseudorapidity-azimuthal angle separation between the boson and the candidate fat jet is negligible. Ensuring a minimal angular distance confirms that both objects are aligned and moving in the same direction.

Figure 4.3 shows the differential cross-section distributions for both the $W^{\pm}$ boson jet mass (m^{JW}) and the backlash QCD jet mass (m^{JB}). For the $W^{\pm}$ boson jet, only a small fraction of events fall below 70 GeV, while a pronounced peak appears near the $W^{\pm}$ boson mass. This peak broadens toward higher masses due to parton shower effects. In contrast, the recoil QCD jet does not exhibit such a distinct peak around 80 GeV.

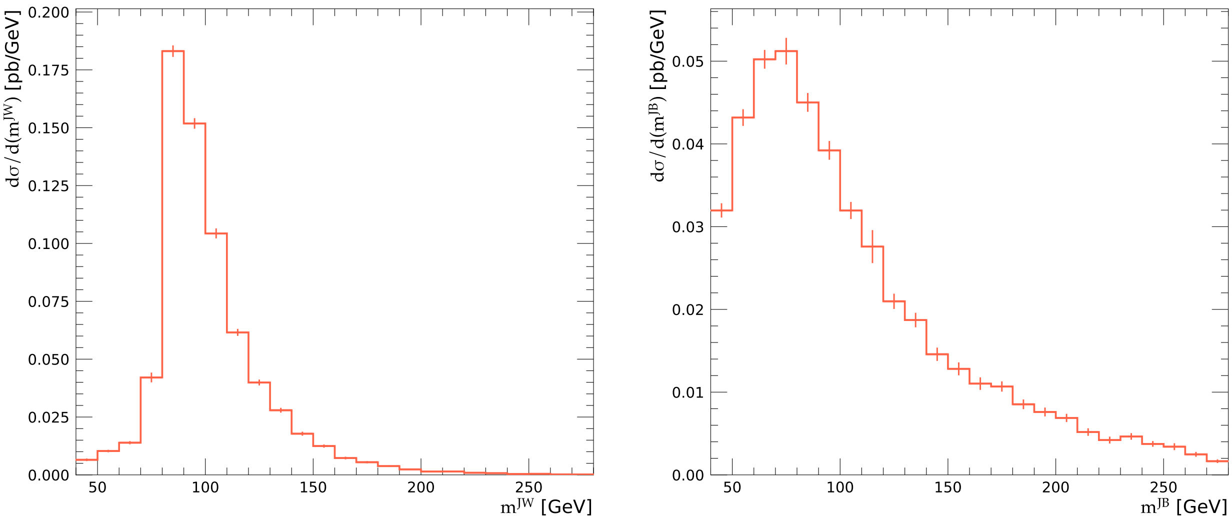

Figure 4.3: Jet masses for the $W^{\pm}$ boson fat jet m^{JW} (left) and the QCD fat jet m^{JB} (right). The jets are identified using truth-level information about the $W^{\pm}$ boson.

These plots motivate the first investigation into discriminating recoil jets from the vector boson jets without relying on truth-level information, which is not available in actual experimental data from detectors.

4.3.1 Mass windows for the fat jets

Because the $W^{\pm}$ boson jet mass exhibits a distinctively peaked distribution, one straightforward method to differentiate $W^{\pm}$ boson jets from QCD jets is to define mass windows centered on the $W^{\pm}$ mass. To test the effectiveness of this approach, four increasingly narrow mass intervals are tested. These intervals are compared to a baseline strategy in which the highest p_T fat jet is always chosen as the vector boson jet. Concretely, if an event contains only one fat jet, that jet is selected as the $W^\pm$ boson jet. In events with two fat jets, progressively tighter mass cuts are applied until only one jet remains within the selected mass window. Ideally, this surviving jet can be confidently identified as originating from the $W^\pm$ boson. If no mass window successfully isolates a single candidate, the jet with the highest p_T is again chosen.

cases		**ratio**
One fat jet...	...overall	0.58
	...in mass window 70 GeV to 90 GeV	0.64
	...in mass window 72.5 GeV to 87.5 GeV	0.53
	...in mass window 75 GeV to 85 GeV	0.56
	...in mass window 77.5 GeV to 82.5 GeV	0.50
Two fat jets in all mass windows (guess jet with highest p_T)		0.56

Table 4.2: Identification success rates for various mass window selections. The ratio indicates the fraction of events in which the $W^\pm$ boson jet was correctly identified under each selection scenario.

The effectiveness of the mass window selection method for distinguishing $W^\pm$ boson jets from QCD jets, via the truth-level information, is presented in table 4.2. Initially, for events containing only one fat jet without any mass window constraints, the single available jet is the $W^\pm$ boson jet in 58% of the events. If there are two fat jets in the event, with a mass window from 70 GeV to 90 GeV, the identification accuracy improves to 64%. This improvement shows the benefit of constraining the jet mass closer to the $W^\pm$ boson mass, thereby enhancing discrimination against QCD jets.

However, as the mass window is further narrowed, the identification efficiency decreases. Narrower mass windows may reduce QCD jet contamination, but also increase the probability of excluding genuine $W^\pm$ boson jets.

In events where two fat jets are present, that cannot be distinguished by mass windows, the jet with the highest transverse momentum is chosen. This approach yields a correct identification ratio slightly lower than the identification rate achieved with the broadest mass window, suggesting that mass window cuts can only provide a rather small improvement in discrimination performance.

As demonstrated above, this technique provides an initial foundation for further studies. However, it does not sufficiently ensure the reliable identification of the $W^\pm$ fat jet when employed alone. Consequently, an alternative method is investigated in the following section.

4.3.2 Fox-Wolfram moments

To analyze the Fox-Wolfram moments for jets, as defined in eq. (3.3), it is necessary to perform a Lorentz boost to the center-of-mass frame of the jet. In this frame, a $W^{\pm}$ boson jet has a two-pronged structure with quarks emitted back-to-back [18].

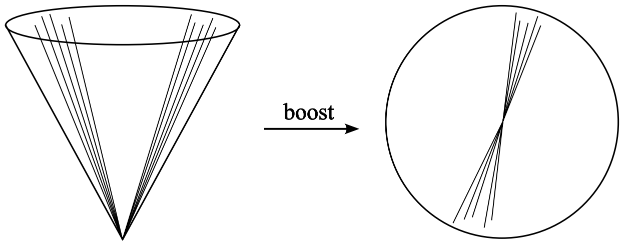

Figure 4.4: Schematic of a fat jet with two sub-jets in the lab frame (left) and boosted to its center-of-mass frame (right) [18].

For such jets, due to the symmetric angular distribution about the jet axis, the first moment H_1 is expected to be approximately zero, while H_0 and H_2 are expected to be close to one. In contrast, QCD jets typically show a single-pronged more isotropic structure. This leads to higher values of H_1 due to asymmetries and lower values of H_2 compared to $W^{\pm}$ boson jets. The ratio between H_0 and H_2, denoted as R^2, serves as a discriminating variable.

Following the approach of ref. [18], the objective is to differentiate QCD jets from $W^{\pm}$ boson jets using the distribution of R^2. The corresponding histograms for this analysis are shown in fig. 4.5. Noticeably the histograms do not precisely align with the results shown in ref. [18].

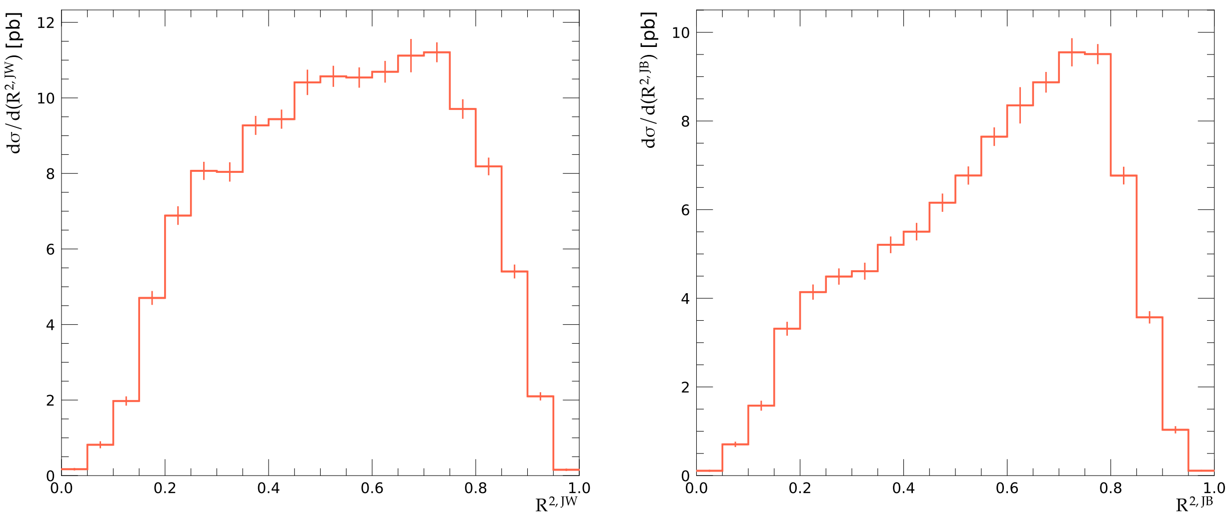

Figure 4.5: Differential cross section for R^2 of the $W^{\pm}$ boson fat jet (left) and the QCD fat jet (right).

For $W^{\pm}$ boson jets (left histogram), the R^2 differential cross section closely matches the expected distribution, exhibiting a peak at higher R^2 values. However, the differential cross section below $R^2 = 0.5$ is larger than anticipated. The differential cross section for the recoil QCD jet does not confirm the expectations. QCD jets are anticipated to peak at lower R^2 values, but the observed distribution peaks at higher values.

Possible reasons for these discrepancies include the applied jet clustering method and its settings. The anti-k_t clustering algorithm used to reconstruct jets may incorrectly merge particles into fat jets, thereby affecting the value of R^2. This could lead to a broadening of the R^2 distribution for $W^{\pm}$ boson jets. Additionally, particles that do not belong to the actual two-pronged structure may be included, making the jets appear more isotropic. Another potential cause is that the selection criteria for the fat jets might preferentially include QCD jets with high R^2. Another crucial point to note is that the conditions employed in this study are not identical to those presented in the mentioned paper ([18]). For instance, the anti-k_t jet clustering algorithm utilized a radius parameter of 0.6, a p_T cut of 80 GeV, and a mass window for the $W^{\pm}$ boson jet spanning from 40 GeV to 140 GeV.

Therefore, an effective discrimination between $W^{\pm}$ boson jets and QCD jets for this study requires a multifaceted approach. Incorporating additional substructure variables and employing machine learning algorithms could improve the identification performance.

5 Polarization studies

This chapter presents studies on polarized simulations of massive vector bosons undergoing hadronic decays. Initially, an overview of the production rates for the vector bosons and their polarization states is provided. Subsequently, the properties of the jets from polarized $W^\pm$ and Z bosons and their associated substructure variables are examined. These studies are conducted on events featuring hadronically decaying $W^\pm$ and Z bosons with up to one additional jet at NLO and up to three jets at LO, as detailed in B.

5.1 Integrated polarized cross sections

In this section, the contributions of different polarization states of massive vector bosons to the unpolarized cross section are examined. The unpolarized cross section comprises the transverse (T) and longitudinal (0) polarization cross sections, as well as the interference (coint) between these components. It is important to note that the transverse polarization component already includes the interference between left- and right-handed circular polarization states [16].

Table 5.1 presents the integrated cross sections for the polarization components of the $W^\pm$ and Z bosons at generation level. For each boson, the transverse, longitudinal, and interference contributions to the cross section are listed, along with their corresponding statistical uncertainties. Interestingly, the cross section for the W^+ boson is approximately 1.6 times

		integrated cross section			
		transverse [pb]	**longitudinal** [pb]	**interference** [pb]	**unpolarized** [pb]
Boson	W^+	80.25 ± 0.05	5.095 ± 0.008	0.01 ± 0.02	85.36 ± 0.08
	W^-	49.76 ± 0.03	3.070 ± 0.005	0.005 ± 0.009	52.84 ± 0.04
	Z	54.69 ± 0.04	3.938 ± 0.005	$-(0.013 \pm 0.007)$	58.62 ± 0.05

Table 5.1: Polarized cross sections at generation level for $W^\pm$ or Z boson production with up to one additional jet at NLO and up to three jets at LO.

higher than that for the W^- boson. Intuitively, a factor of two might be expected, given that protons contain twice as many up quarks as down quarks. However, interactions between quarks and gluons within protons lead to this discrepancy. Protons are dynamic systems in which virtual gluons are continuously exchanged by strongly interacting quarks, which can fluctuate into virtual quark-antiquark pairs. As a result, protons are composed not only of their valence quarks (uud) but also of sea quarks. The probability of finding a particular parton carrying a specific momentum fraction of the proton is described by the parton distribution function (PDF) [2]. Consequently, due to the significant contribution from sea quarks, the ratio of W^+ to W^- boson production is observed to be lower than two.

Additionally, it is noteworthy that the transverse polarization state dominates over the longitudinal one. In table 5.2 the polarization fractions, defined as the ratio of polarized cross section to unpolarized cross section, is shown for the $W^\pm$ or Z boson production with an associated jet.

		polarization fractions		
		transverse [%]	**longitudinal** [%]	**interference** [%]
Boson	W^+	94.01 ± 0.11	5.97 ± 0.01	0.01 ± 0.02
	W^-	94.17 ± 0.09	5.81 ± 0.01	0.01 ± 0.02
	Z	93.30 ± 0.10	6.72 ± 0.01	$-(0.02 \pm 0.01)$

Table 5.2: Polarization fractions at generation level for $W^\pm$ or Z boson production with up to one additional jet at NLO and up to three jets at LO.

It can be seen, that the longitudinal polarization fractions are small compared to the transverse polarization fractions. This effect can be described by the Goldstone equivalence theorem. According to this theorem, the longitudinal polarization component effectively vanishes for highly boosted vector bosons because the associated Goldstone bosons cannot couple to light quarks [23]. This behavior is closely related to the electroweak symmetry breaking mechanism, where the longitudinal modes of the massive vector bosons are related to the Goldstone bosons that emerge from spontaneous symmetry breaking. It is noticeable that the longitudinal polarization fraction of the Z boson is higher than for the $W^\pm$ bosons. This is also an effect of the Goldstone equivalence theorem, because the Z boson is heavier and therefore less suppressed at the same energies.

5.2 Polarized vector boson jets

As seen in the previous section, the W^+ boson production has the highest cross section and therefore will be used as a representative in the upcoming studies. For W^- and Z boson jets similar observations could be made.

5.2.1 Effects on jet constituents

The polarization state of a vector boson influences the kinematic properties of its decay products, which in turn affects the jet substructure. When the boson is longitudinally polarized, its spin is perpendicular to its direction of motion, causing the decay products to be more collimated along that axis. In contrast, a transverse polarization, where the spin is aligned with the boson's direction of travel, results in a broader angular distribution of the decay products [24].

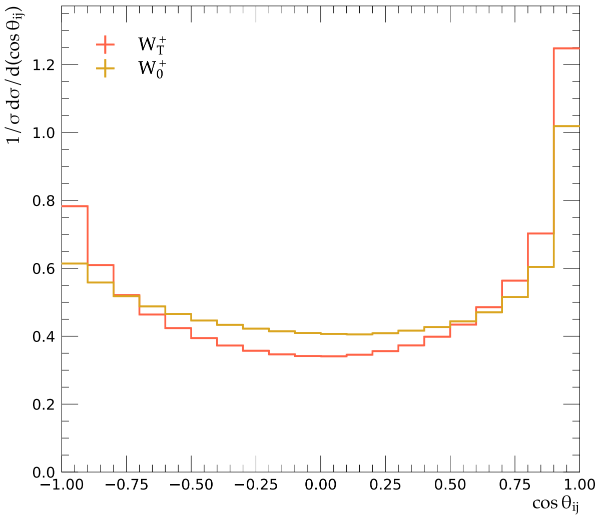

Figure 5.1: Normalized differential cross section of the cosine of the angle between the momenta of the jets constituents i and j for transverse and longitudinal polarized W^+ boson in the center-of-mass frame of the jet. The interference term is not shown because of the required normalization.

Figure 5.1 presents the normalized differential cross section for longitudinally and transversely polarized W^+ boson jets, plotted as a function of the cosine of the angle between the momenta of each jet constituent i and every other jet constituent j in the center-of-mass frame of the jet. Due to the much lower production rate of longitudinally polarized bosons compared to transversely polarized ones, the cross section has been normalized to unity to facilitate comparison of the shapes. By definition, values of $+1$ and -1 correspond to constituents moving parallel and antiparallel to another, respectively. Particles emitted back-to-back in the center-of-mass frame move in different directions in the laboratory frame. Conversely, particles moving parallel in the center-of-mass frame are observed in the same direction after boosting to the lab frame, as illustrated in fig. 4.4.

The differential cross sections for longitudinal polarization state shows reduced probabilities near -1 and 1 and enhanced probabilities around 0 when compared to the transverse polarization state. This suggests fewer pairs of particles are aligned into distinct sub-jet-like structures, resulting in a more isotropic momentum distribution within the fat jet.

5.2.2 Substructure variables

In this section, the effects of different polarization states of vector bosons on the substructure variables of vector boson jets are examined. A selection based on variables commonly used for vector boson jet tagging is employed. The plots for W^+ bosons are presented in fig. 5.2, while those for W^- and Z bosons are provided in appendix A. To enhance visibility, the cross sections for the longitudinal and interference components are scaled by a factor of ten.

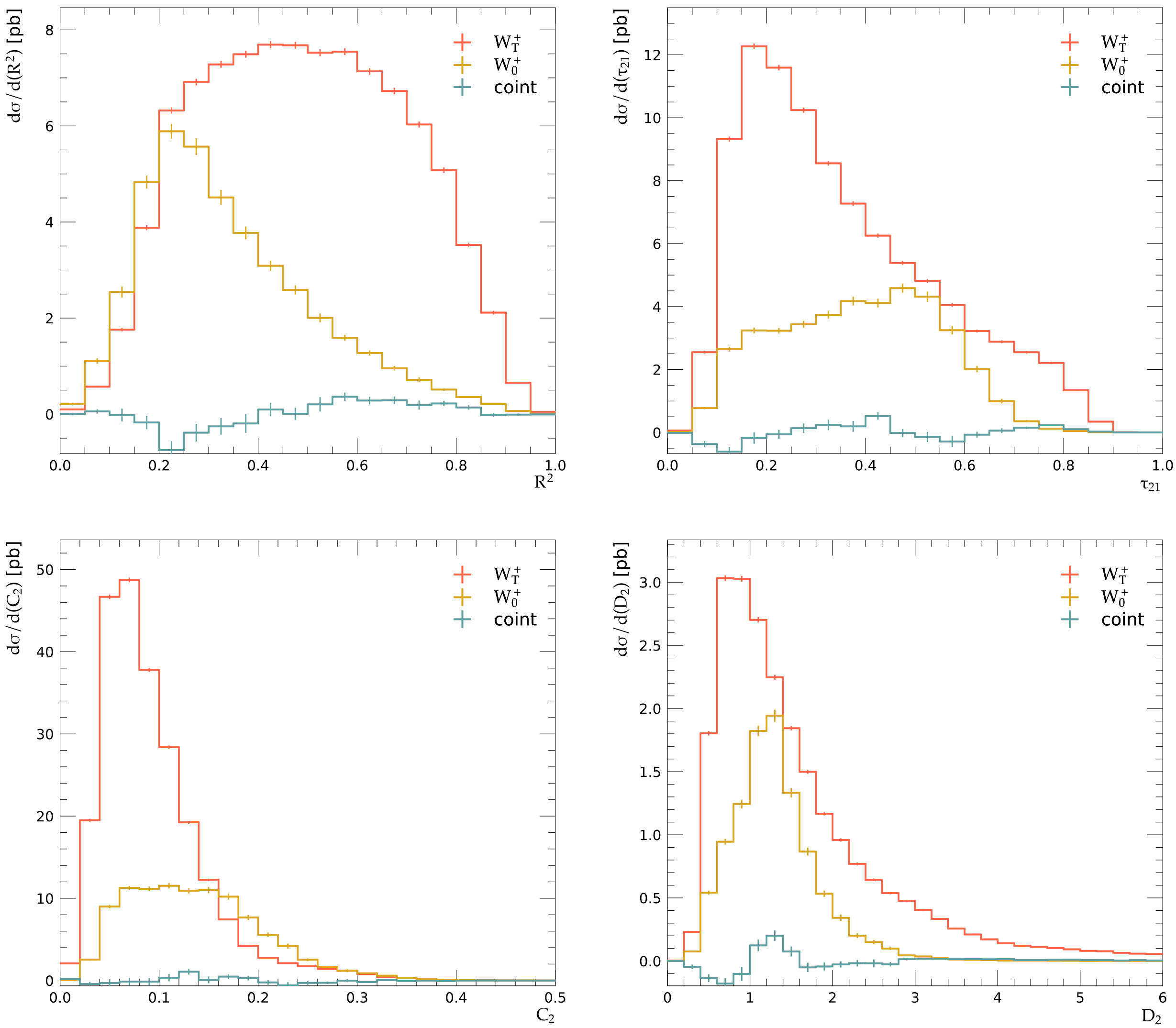

Figure 5.2: Substructure variables for the longitudinally and transversely polarized W^+ boson jet and their interference term. Top left: R^2; top right: τ_{21}; bottom left: C_2; bottom right: D_2. The differential cross sections for W_0^+ and coint are scaled by a factor of ten.

Fox-Wolfram moments

The Fox-Wolfram moments H_l, discussed in section 4.3.2, are investigated with respect to the polarization of vector bosons. In this analysis, the ratio $R^2 = H_2/H_0$ is specifically evaluated for vector boson jets. The top-left panel of fig. 5.2 presents the cross section of R^2 for W^+ bosons with transverse (red) and longitudinal (yellow) polarizations, alongside the interference term (blue).

For transversely polarized W^+ bosons, the R^2 distribution exhibits a relatively uniform profile for values between 0.2 and 0.8. This behavior aligns with that of unpolarized vector boson jets, as depicted in fig. 4.5. However, this characteristic uniformity implies that the substructure of transversely polarized jets does not favor any particular angular configuration, leading to a diverse range of distribution patterns within the jet. Consequently, the Fox-Wolfram moments and the R^2 ratio may not be practical for identifying two-prong structures within the experimental setup of this thesis. In contrast, longitudinally polarized W^+ bosons display a significantly different R^2 distribution. A pronounced peak emerges at lower R^2 values, where H_0 exceeds H_2. This peak is indicative of a more isotropic and uniform substructure within the jet, suggesting that longitudinally polarized bosons tend to produce jets with an isotropic distribution of constituents. The dominance of H_0 over H_2 at lower R^2 values highlights the reduced angular complexity in the jet's particle distribution. The interference term, represented in blue, contributes to the overall R^2 distribution by accounting for the quantum mechanical mixing between different polarization states.

These observations underscore the sensitivity of the Fox-Wolfram moments, and specifically the R^2 ratio, to the polarization states of vector boson jets. While R^2 may not offer significant discrimination power for separating QCD jets from $W^\pm$ boson jets within the context of this study, it emerges as a potent tool for probing the polarization characteristics of highly boosted fat jets. The distinct behavior of R^2 across different polarization states suggests that it can complement other substructure variables in constructing a more comprehensive toolkit for jet tagging and polarization analysis.

N-subjettiness

The variable $\tau_{21} = \tau_2/\tau_1$ quantifies the ratio of 2-subjettiness to 1-subjettiness, serving as a key observable in jet substructure analysis. As defined in eq. (3.4), N-subjettiness measures the extent to which a jet can be effectively decomposed into N distinct sub-jets. Specifically, jets with small values of τ_2 combined with large values of τ_1 are indicative of a two-pronged substructure, suggesting the presence of two sub-jets within the jet. Conversely, jets exhibiting large values for both τ_1 and τ_2 tend to display a more isotropic or single-pronged substructure, lacking distinct sub-jets [19].

In the top right panel of fig. 5.2, the differential cross sections for τ_{21} are illustrated. The analysis reveals that jets originating from transversely polarized vector bosons exhibit a pronounced peak at lower τ_{21} values, confirming their two-pronged jet structure. In contrast, jets from longitudinally polarized vector bosons display a relatively flat distribution at smaller

τ_{21} values and a less prominent peak at $\tau_{21} \approx 0.5$. This behavior suggests a more isotropic and single-pronged substructure for longitudinally polarized boson jets.

These observations underscore the sensitivity of τ_{21} to the polarization states of vector boson jets. By effectively differentiating between two-pronged and isotropic jet structures, τ_{21} serves as a powerful tool for identifying and characterizing the polarization of vector bosons in high-energy collisions.

Transverse momentum correlation functions

Transverse momentum correlation functions, as defined in eq. (3.6), are used to quantify the correlations between the transverse momenta of particles within a jet. In systems containing N sub-jets, it is typically observed that the energy correlation function $ECF(N+1)$ is significantly smaller than $ECF(N)$ [20]. This property enables the investigation of jet substructure by allowing the examination of transverse momentum correlations for varying numbers of constituents.

To effectively characterize these correlations, the following ratios are introduced:

$$e_2 = \frac{ECF(2)}{(ECF(1))^2} \quad \text{and} \quad e_3 = \frac{ECF(3)}{(ECF(1))^3}. \tag{5.1}$$

Here, e_2 and e_3 are defined as normalized measures of two-particle and three-particle transverse momentum correlations, respectively. These ratios provide a framework for comparing different orders of momentum correlations within the jet.

Building upon these fundamental ratios, the substructure variables C_2 and D_2 are constructed as follows:

$$C_2 = \frac{e_3}{(e_2)^2} \quad \text{and} \quad D_2 = \frac{e_3}{(e_2)^3}. \tag{5.2}$$

The variable C_2 is the three-particle transverse momentum correlation normalized by the square of the two-particle correlation. This normalization enhances the sensitivity of C_2 to three-particle interactions within the jet.

The differential cross sections for C_2 are depicted in the bottom left panel of fig. 5.2. These distributions exhibit pronounced sensitivity to the polarization state of the originating vector boson. For transversely polarized W^+ bosons, a distinct peak is observed near $C_2 \approx 0.08$, followed by a rapid decline, resulting in a significantly reduced cross section by $C_2 \approx 0.2$. This behavior is characteristic of fat jets containing two sub-jets [20]. In contrast, longitudinally polarized W^+ bosons display a less pronounced peak around $C_2 \approx 0.12$, with a broader distribution extending to higher C_2 values. This broader distribution suggests a less prominent two-prong structure, potentially indicating a more isotropic or diffuse internal configuration of the jet constituents.

The variable D_2 is further utilized to enhance sensitivity to three-particle transverse momentum correlations by normalizing e_3 to the cube of e_2 [25]. Unlike C_2, which is bounded between zero and one, D_2 is capable of exceeding one. The differential cross sections for D_2 are illustrated in the bottom right panel of fig. 5.2. Notably, the peak for transversely polarized W^+ bosons occurs at lower D_2 values compared to longitudinally polarized W^+ bosons. This observation aligns with the expected behavior for one-prong and two-prong jets as described in the literature, thereby confirming that D_2 effectively discriminates between different jet substructure topologies [25].

Overall, both C_2 and D_2 effectively discriminate between transversely and longitudinally polarized vector bosons by highlighting differences in their internal jet substructures.

6 Summary and outlook

This thesis is dedicated to the simulation and analysis of polarized massive vector bosons undergoing hadronic decays, with the primary objective of evaluating how different polarization states influenced the resulting jet structures. The polarization of vector bosons dictated the kinematic properties of their decay products, which in turn affected the observable characteristics of the jets formed in high-energy collisions. By investigating these effects, the study aimed to identify key observables that could effectively distinguish between various polarization states. However, achieving this objective required addressing the complexities of these processes.

The kinematic structure of processes involving massive vector bosons was found to be complex, often characterized by high jet multiplicities. This complexity posed significant challenges in distinguishing jets originating from vector bosons from recoil QCD jets when attempting to identify highly boosted vector bosons. To address this, the thesis explored strategies for enhancing the identification of vector boson jets. It was observed that constraining the mass of a vector boson fat jet to a relatively broad mass window (70 to 90 GeV) improved the ability to distinguish these jets from QCD jets; however, further narrowing the mass window resulted in a reduction in discrimination power.

The examination of jet substructure variables was potentially useful for differentiating between jets originating from vector bosons and those from single gluons or quarks. Initial studies revealed that the Fox-Wolfram moments, when analyzed in the center of mass frame of the fat jet, were insufficient for reliably discriminating between vector boson jets and QCD jets within the specific setup of this thesis. Consequently, the evaluation of additional jet substructure variables for this discrimination task is proposed as a direction for future research.

Analyses of cross sections at different orders of perturbation theory indicated that the central ATLAS sample could be reconstructed using a reduced number of NLO and LO jets in the hard process. Furthermore, simulating a relatively small number of jets beyond the LO process enhanced the accuracy of the reconstruction compared to simulations that only included the LO process.

In the final section of this thesis, polarized simulations of massive vector bosons were analyzed. Cross sections for different polarization states were studied, revealing that the production rate ratio of W^+ to W^- was lower than the expected value of two. This reduction was attributed to the contribution of sea quarks from the colliding protons. Additionally, an important finding was the predominance of the transverse polarization state over the longitudinal polarization state. This predominance was explained by the Goldstone boson equivalence theorem, which accounted for the suppression of the longitudinal polarization state in highly boosted massive vector bosons.

A central focus of this thesis was the influence of different polarization states of vector bosons on their corresponding jets. The objective was to identify observables that were sensitive to polarization and could be measured experimentally. Initially, it was essential to determine how the polarization of the vector boson affected the kinematic properties of its decay products and whether this influenced the measurable jet constituents. This was achieved by analyzing the cosine of the angle between the momenta of particle pairs in the center-of-mass frame of the jet, considering all particles within the reconstructed jet. It was observed that jets originating from longitudinally polarized vector bosons exhibited a more isotropic distribution of constituents, whereas jets from transversely polarized vector bosons displayed a mostly two-pronged structure.

Jet substructure variables were considered ideal for this study due to their sensitivity to differences in jet structure arising from the comparison of longitudinal and transverse polarization states of the vector boson. Commonly used jet substructure variables in vector boson jet tagging were analyzed for this purpose. These observables all exhibited varying degrees of sensitivity to the polarization of the vector boson. Specifically, the variables R^2 and τ_{21} were observed to display more distinct shapes for different polarization states. Additionally, differentiation between polarization states was noticeable for variables related to transverse momentum correlation functions, C_2 and D_2, although the distinctions were not as pronounced as those for the previously mentioned variables.

Future research can enhance the discrimination between vector boson jets and QCD jets by exploring additional jet substructure variables that may offer greater sensitivity to their distinct features. Investigating different transverse momentum cuts at the generation level could optimize the selection of highly boosted vector bosons, improving discrimination power from QCD jets.

Additionally, testing alternative jet clustering algorithms and varying their parameters may lead to more accurate jet reconstruction and classification. Exploring new frames of reference for defining helicity states could provide new insights into the characterization of vector boson polarization, influencing the resulting jet substructures.

Finally, studying the correlations between substructure variables that distinguish vector boson jets from QCD jets and those sensitive to polarization will help develop unbiased tagging methods. These advancements will contribute to more reliable and efficient identification of vector boson jets in high-energy physics experiments.

7 Bibliography

[1] *Largest machine*, https://www.guinnessworldrecords.com/ world-records/ 103591-largest-machine.html, (visited on 12/17/2024).

[2] M. Thomson, *Modern particle physics* (Cambridge university press, Cambridge, 2013).

[3] *Standard Model*, Page Version ID: 1248676010, Sept. 2024, https://en.wikipedia.org/w/index.php?title=Standard_Model&oldid=1248676010.

[4] S. Navas et al., "Review of particle physics", Phys. Rev. D **110**, 030001 (2024) 10.1103/PhysRevD.110.030001.

[5] ATLAS Collaboration, "Measurement of the cross-section of high transverse momentum vector bosons reconstructed as single jets and studies of jet substructure in *pp* collisions at $\sqrt{s} = 7$ TeV with the ATLAS detector", New Journal of Physics **16**, 113013 (2014) 10.1088/1367-2630/16/11/113013, arXiv:1407.0800 [hep-ex].

[6] H. Bartosik and G. Rumolo, *Performance of the LHC injector chain after the upgrade and potential development*, arXiv:2203.09202 [physics], Mar. 2022, http://arxiv.org/abs/2203.09202.

[7] *The accelerator complex*, https://home.cern/science/accelerators/accelerator-complex (visited on 10/20/2024).

[8] *LHC the guide FAQ | CERN*, https://home.cern/resources/brochure/knowledge-sharing/lhc-facts-and-figures (visited on 10/20/2024).

[9] *Detector & Technology*, https://atlas.cern/Discover/Detector (visited on 10/20/2024).

[10] R. M. Bianchi and ATLAS Collaboration, "ATLAS experiment schematic or layout illustration", 2022, https://cds.cern.ch/record/2837191.

[11] I. Neutelings, *CMS coordinate system*, July 2024, https://tikz.net/axis3d_cms/ (visited on 10/20/2024).

[12] I. Neutelings, *Pseudorapidity*, Aug. 2021, https://tikz.net/axis2d_pseudorapidity/ (visited on 10/20/2024).

[13] SHERPA Team, *Sherpa Homepage — Sherpa documentation*, https://sherpa-team.gitlab.io/ (visited on 10/21/2024).

[14]Rivet Team, *Rivet — the particle-physics MC analysis toolkit – Hepforge*, `https://rivet.hepforge.org/` (visited on 12/06/2024).

[15]J. Campbell, J. Huston, and F. Krauss, *The black book of quantum chromodynamics: a primer for the LHC era*, First edition (Oxford University Press, Oxford, 2018).

[16]M. Hoppe, M. Schönherr, and F. Siegert, "Polarised cross sections for vector boson production with Sherpa", Journal of High Energy Physics **2024**, 1 (2024) `10.1007/JHEP04(2024)001`, `https://link.springer.com/10.1007/JHEP04(2024)001`.

[17]M. Cacciari, G. P. Salam, and G. Soyez, "The anti-k_t jet clustering algorithm", Journal of High Energy Physics **2008**, 063–063 (2008) `10.1088/1126-6708/2008/04/063`, arXiv:`0802.1189 [hep-ph]`.

[18]C. Chen, "New approach to identifying boosted hadronically-decaying particle using jet substructure in its center-of-mass frame", Physical Review D **85**, arXiv:1112.2567 [hep-ph], 034007 (2012) `10.1103/PhysRevD.85.034007`, `http://arxiv.org/abs/1112.2567`.

[19]J. Thaler and K. V. Tilburg, "Identifying Boosted Objects with N-subjettiness", Journal of High Energy Physics **2011**, arXiv:1011.2268 [hep-ph], 15 (2011) `10.1007/JHEP03(2011)015`, `http://arxiv.org/abs/1011.2268`.

[20]A. J. Larkoski, G. P. Salam, and J. Thaler, "Energy Correlation Functions for Jet Substructure", Journal of High Energy Physics **2013**, arXiv:1305.0007 [hep-ph], 108 (2013) `10.1007/JHEP06(2013)108`, `http://arxiv.org/abs/1305.0007`.

[21]ATLAS Collaboration, "Measurement of jet-substructure observables in top quark, W boson and light jet production in proton-proton collisions at $\sqrt{s} = 13$ TeV with the ATLAS detector", Journal of High Energy Physics **2019**, arXiv:1903.02942 [hep-ex], 33 (2019) `10.1007/JHEP08(2019)033`, `http://arxiv.org/abs/1903.02942`.

[22]ATLAS Collaboration, *Wqq_ptw_200_ecms.py · master · atlas-physics / pmg / MC Job Options · GitLab*, May 2023.

[23]Z. Bern et al., "Left-Handed W Bosons at the LHC", Physical Review D **84**, arXiv:1103.5445 [hep-ph], 034008 (2011) `10.1103/PhysRevD.84.034008`, `http://arxiv.org/abs/1103.5445`.

[24]C. Bittrich, "Study of Polarization Fractions in the Scattering of Massive Gauge Bosons $W^{\pm}Z \to W^{\pm}Z$ with the ATLAS Detector at the Large Hadron Collider",

[25]A. J. Larkoski, I. Moult, and D. Neill, "Power Counting to Better Jet Observables", Journal of High Energy Physics **2014**, arXiv:1409.6298 [hep-ph], 9 (2014) `10.1007/JHEP12(2014)009`, `http://arxiv.org/abs/1409.6298`.

A Additional plots

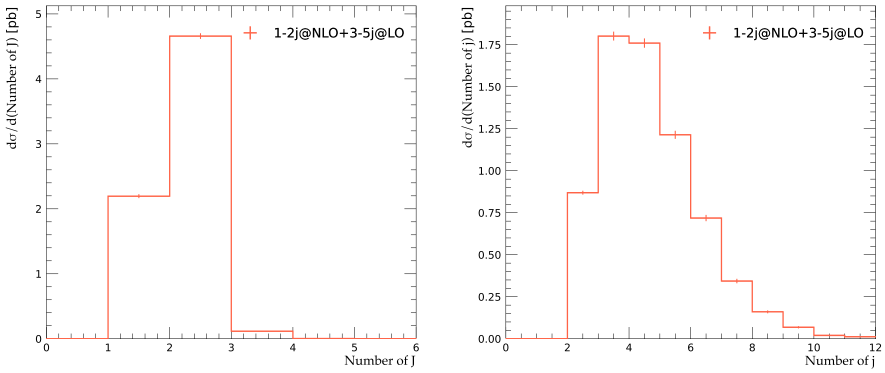

Figure A.1: Number of fat jets (left) and small jets (right) for the central ATLAS sample.

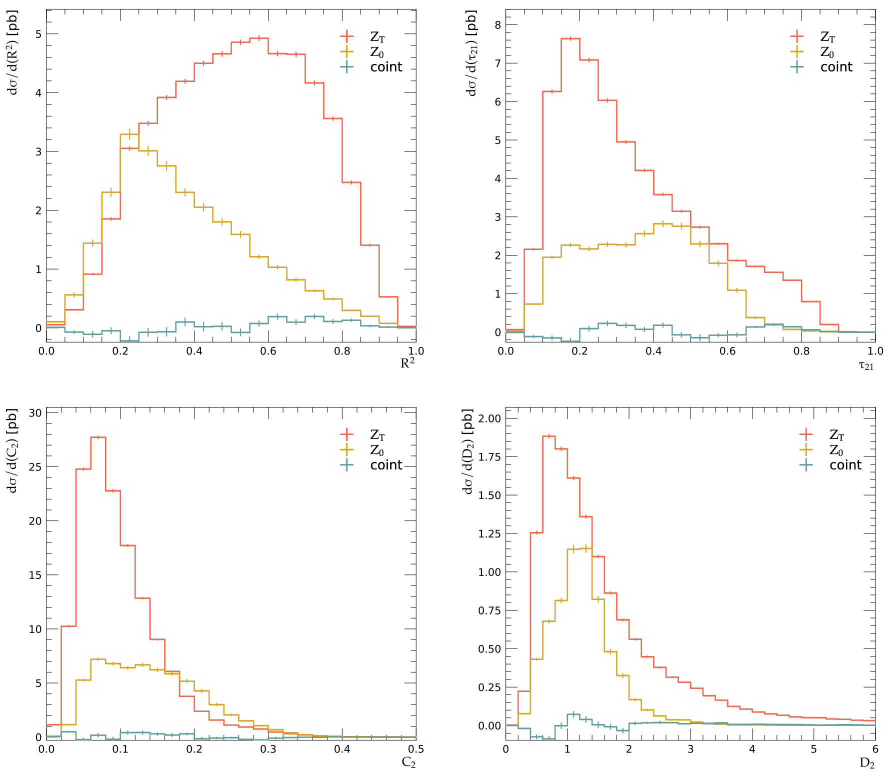

Figure A.2: Different substructure variables for the polarized Z boson jet. The differential cross sections for Z_0 and coint are scaled by a factor of ten for better visabilty.

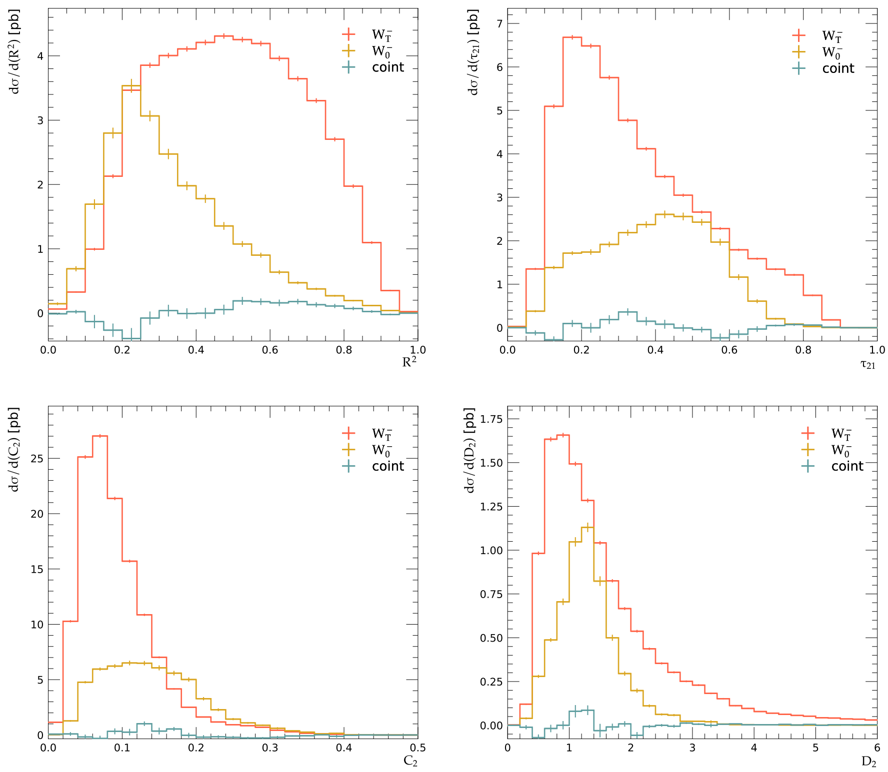

Figure A.3: Different substructure variables for the polarized W^- boson jet. The differential cross sections for W_0^- and coint are scaled by a factor of ten for better visabilty.

B Run-Cards

W[qq] + 1Jet@LO unpolarized

```
# Sherpa configuration for W[hadrons]+1j@LO production
# set up beams for LHC run 2
BEAMS: 2212
BEAM_ENERGIES: 6500
# matrix-element calculation
ME_GENERATORS: [Comix]
# set Fermi constant
GF: 0.00001166397
# set PDF
PDF_LIBRARY: LHAPDFSherpa
PDF_SET: NNPDF30_nnlo_as_0118_hessian
ALPHAS: {USE_PDF: 1}
# set the width of W and Z to zero
PARTICLE_DATA:
  24:
    Width: 0.0
  23:
    Width: 0.0
# to be consistent with setting all VB widths to zero
WIDTH_SCHEME: Fixed
# enforce all possible hadronic hard decays of the W bosons
HARD_DECAYS:
  Enabled: true
  Channels:
    24,2,-1:  {Status: 2}
    24,4,-3:  {Status: 2}
    -24,-2,1: {Status: 2}
    -24,-4,3: {Status: 2}

PROCESSES:
- 93 93 -> 24 93:
    Order: {QCD: 1, EW: 1}
- 93 93 -> -24 93:
    Order: {QCD: 1, EW: 1}
# only boosted jets of the W bosons
```

```
SELECTORS:
- [PT, 24, 200.0, E_CMS]
- [PT, -24, 200.0, E_CMS]
# write out hepmc data
EVENT_OUTPUT: HepMC3_GenEvent[Events/events$(ID).hepmc]
```

W[qq] + 1j@NLO + 2-3j@LO unpolarized

```
# Sherpa configuration for W[hadrons]+1j@NLO2-3j@LO production
# set up beams for LHC run 2
BEAMS: 2212
BEAM_ENERGIES: 6500
# matrix-element calculation
ME_GENERATORS:
- Comix
- Amegic
- OpenLoops
# set Fermi constant
GF: 0.00001166397
PDF_LIBRARY: LHAPDFSherpa
PDF_SET: NNPDF30_nnlo_as_0118_hessian
ALPHAS: {USE_PDF: 1}
# set the width of W and Z to zero
PARTICLE_DATA:
  24:
    Width: 0.0
  23:
    Width: 0.0
# to be consistent with setting all VB widths to zero
WIDTH_SCHEME: Fixed
# enforce all possible hadronic hard decays of the W bosons
HARD_DECAYS:
  Enabled: true
  Channels:
    24,2,-1:  {Status: 2}
    24,4,-3:  {Status: 2}
    -24,-2,1: {Status: 2}
    -24,-4,3: {Status: 2}

PROCESSES:
- 93 93 -> 24 93 93{2}:
    Order: {QCD: 1, EW: 1}
    CKKW: 20
    2->2:
      NLO_Mode: MC@NLO
```

```
      NLO_Order: {QCD: 1, EW: 0}
      ME_Generator: Amegic
      RS_ME_Generator: Comix
      Loop_Generator: OpenLoops
- 93 93 -> -24 93 93{2}:
    Order: {QCD: 1, EW: 1}
    CKKW: 20
    2->2:
      NLO_Mode: MC@NLO
      NLO_Order: {QCD: 1, EW: 0}
      ME_Generator: Amegic
      RS_ME_Generator: Comix
      Loop_Generator: OpenLoops
MC@NLO:
  PSMODE: 2
  #RS_SCALE: VAR{sqr(sqrt(H_T2)-PPerp(p[2])+MPerp(p[2]))/4}
MEPS:
  CLUSTER_MODE: 1384
# only boosted jets of the W bosons
SELECTORS:
- [PT, 24, 200.0, E_CMS]
- [PT, -24, 200.0, E_CMS]
# write out hepmc data
EVENT_OUTPUT: HepMC3_GenEvent[Events/events$(ID).hepmc]
```

W[qq] + 1j@NLO + 2-3j@LO polarized

```
# Sherpa configuration for polarized W[hadrons]+1j@NLO+2-3j@LO production
# set up beams for LHC run 2
BEAMS: 2212
BEAM_ENERGIES: 6500
# matrix-element calculation
ME_GENERATORS:
- Comix
- Amegic
- OpenLoops
COMIX_DEFAULT_GAUGE: 0
# set the width of W and Z to zero
PARTICLE_DATA:
  24:
    Width: 0.0
  23:
    Width: 0.0
# to be consistent with setting all VB widths to zero
WIDTH_SCHEME: Fixed
```

```
# enforce all possible hadronic hard decays of the W bosons
HARD_DECAYS:
  Enabled: true
  Channels:
    24,2,-1:  {Status: 2}
    24,4,-3:  {Status: 2}
  Pol_Cross_Section:
    Enabled: true
    Reference_System: [Lab, COM]

PROCESSES:
- 93 93 -> 24 93 93{2}:
    Order: {QCD: 1, EW: 1}
    CKKW: 20
    2->2:
      NLO_Mode: MC@NLO
      NLO_Order: {QCD: 1, EW: 0}
      ME_Generator: Amegic
      RS_ME_Generator: Comix
      Loop_Generator: OpenLoops
MC@NLO:
  PSMODE: 2
  #RS_SCALE: VAR{sqr(sqrt(H_T2)-PPerp(p[2])+MPerp(p[2]))/4}
MEPS:
  CLUSTER_MODE: 1384
# only boosted jets of the W bosons
SELECTORS:
- [PT, 24, 200.0, E_CMS]
- [PT, -24, 200.0, E_CMS]
# write out hepmc data
EVENT_OUTPUT: HepMC3_GenEvent[Events/events$(ID).hepmc]
```

Z[qq] + 1j@NLO + 2-3j@LO polarized

```
# Sherpa configuration for Z[hadrons]+1j@NLO+2-3j@LO production
# set up beams for LHC run 2
BEAMS: 2212
BEAM_ENERGIES: 6500
# matrix-element calculation
ME_GENERATORS:
- Comix
- Amegic
- OpenLoops
COMIX_DEFAULT_GAUGE: 0
# set the width of W and Z to zero
```

```
PARTICLE_DATA:
  24:
    Width: 0.0
  23:
    Width: 0.0
# to be consistent with setting all VB widths to zero
WIDTH_SCHEME: Fixed
# enforce all possible hadronic hard decays of the Z boson
HARD_DECAYS:
  Enabled: true
  Channels:
    23,1,-1:  {Status: 2}
    23,2,-2:  {Status: 2}
    23,3,-3:  {Status: 2}
    23,4,-4:  {Status: 2}
    23,5,-5:  {Status: 2}
  Pol_Cross_Section:
    Enabled: true
    Reference_System: [Lab, COM]
# hadrons -> Z+1Jet@NLO2,3Jets@LO
PROCESSES:
- 93 93 -> 23 93 93{2}:
    Order: {QCD: 1, EW: 1}
    CKKW: 20
    2->2:
      NLO_Mode: MC@NLO
      NLO_Order: {QCD: 1, EW: 0}
      ME_Generator: Amegic
      RS_ME_Generator: Comix
      Loop_Generator: OpenLoops
MC@NLO:
  PSMODE: 2
  #RS_SCALE: VAR{sqr(sqrt(H_T2)-PPerp(p[2])+MPerp(p[2]))/4}
MEPS:
  CLUSTER_MODE: 1384
# only boosted jets of the Z bosons
SELECTORS:
- [PT, 23, 200.0, E_CMS]
# write out hepmc data
EVENT_OUTPUT: HepMC3_GenEvent[Events/events$(ID).hepmc]
```

C Selbstständigkeitserklärung

Hiermit erkläre ich, Max Lehmann, diese Bachelor-Arbeit im Rahmen der Betreuung am Institut für Kern- und Teilchenphysik ohne unzulässige Hilfe Dritter verfasst und alle Quellen als solche gekennzeichnet habe.

Diese Arbeit wurde noch nicht in gleicher oder ähnlicher Form im Rahmen einer anderen Prüfungsleistung vorgelegt.

Max Lehmann
Dresden, Dezember 2024